



Radial anisotropy and S-wave velocity depict the internal to external zones transition within the Variscan orogen (NW Iberia)

Jorge Acevedo¹, Gabriela Fernández-Viejo¹, Sergio Llana-Fúnez¹, Carlos López-Fernández¹, Javier Olona² and Diego Pérez-Millán¹

5 ¹Department of Geology, University of Oviedo. Arias de Velasco st., 33005, Oviedo, Spain

²TerraDat España, 113 Cristo de las Cadenas Av., 33006, Oviedo, Spain

Correspondence to: Jorge Acevedo (acevedojorge@uniovi.es)

Abstract. The cross-correlation of ambient noise records registered by seismic networks has proven to be a valuable tool to obtain new insights into the crustal structure at different scales. Based on 2- to 14-s-period Rayleigh and Love dispersion data extracted from the seismic ambient noise recorded by 20 three-component broadband stations belonging to two different temporary experiments, we present the first i) upper crustal (1-14 km) high-resolution shear wave velocity and ii) radial anisotropy variation models of the continental crust in NW Iberia. The area of study represents one of the best exposed cross-sections along the Variscan orogen of western Europe, showing the transition between the external eastern zones towards the internal areas in the west. Both the 2-D maps and an E-W transect reveal a close correspondence with the main geological domains of the Variscan orogen. The foreland-fold and thrust-belt of the orogen, the Cantabrian Zone, is revealed by a zone of relatively low shear wave velocities (2.3-3.0 km/s), while the internal zones generally display higher homogeneous velocities (> 3.1km/s). The boundary between both zones is clearly delineated in the models, depicting the arcuate shape of the orogen grain. The velocity patterns also reveal variations of the bulk properties of the rocks that can be linked to major Variscan structures, such as the basal detachment of the Cantabrian Zone or the stack of nappes involving pre-Variscan basement; or sedimentary features such as the presence of thick syn-orogenic siliciclastic wedges. Overall, the radial anisotropy magnitude varies between -5 and 15 % and increases with depth. The depth pattern suggests that the alignment of cracks is the main source of anisotropy at < 8 km depths, although the intrinsic anisotropy seems to be significant in the West-Asturian Leonese Zone, the low-grade slate belt adjacent to the Cantabrian Zone. At depths > 8 km, widespread high and positive radial anisotropies are observed, caused by the presence of subhorizontal alignments of grains and minerals in relation to the internal deformation of rocks either during the Variscan orogeny or prior to it.

1 Introduction

Seismic anisotropy is a ubiquitous feature within the Earth's interior that provides valuable information about the fabric of the geological materials and the tectonic and geodynamic processes causing it (Dreiling *et al.* 2018). It is usually investigated through laboratory tests on rock samples (e.g. Godfrey *et al.*, 2000; Ji *et al.*, 2015) or estimated indirectly from the direction-dependent velocity variation of the seismic waves travelling across a rock formation (e.g., Luo *et al.*, 2013,



Shapiro *et al.*, 2004; Moschetti *et al.*, 2010). Vertically (V_{sv}) and horizontally (V_{sh}) polarized shear waves can be extracted from Rayleigh and Love dispersion measurements, respectively. When $V_{sh} > V_{sv}$, the anisotropy is considered to be positive, whereas when $V_{sv} > V_{sh}$ the anisotropy is negative. Within an isotropic medium, V_{sv} and V_{sh} are equal. However, numerous studies in several locations worldwide have observed the so-called ‘Rayleigh-Love discrepancy’ (Anderson, 1961), which
35 implies that the Rayleigh and Love wave dispersion curves cannot be simultaneously fitted under the assumption of isotropic wave velocities. Following Anderson (1961), this mismatch indicates that the medium is radially anisotropic.

Crustal radial anisotropy (RA) is originated by a variety of source mechanisms whose importance varies with depth. In the shallow crust (<5-10 km) the RA is believed to be caused by crack networks and fractures linked to the regional stress-field (e.g. Crampin *et al.*, 2015). The presence of structure-oriented cracks, bedding planes or grain boundary alignments
40 within the rockmass (e.g. Almqvist and Mainprice, 2017; Boness and Zoback, 2006; Zinke and Zoback, 2000) can also play an important role in the anisotropy from shape-preferred orientation or mineral grains. At pressures higher than 150-200 MPa, equivalent to 6-8 km depth, the increasing lithostatic pressure forces the closure of the cracks and texture-related anisotropy becomes dominant (e.g. Ji *et al.*, 2015; Kern, 1990; Christensen 1985). This type of anisotropy arises from the alignment of minerals with a crystallographic preferred orientation, due to deformation associated to faults and shear zones
45 (Barruol and Kern, 1996). Thus, the effect of this progressive shift in the features that govern the anisotropy is expected to be observed by geophysical methods targeting the upper 10 km of the crust, considering that the shallowest part is sensitive to the properties of the fractures within the rock massif, while the deepest sectors are more susceptible to mineral orientation in the rocks. The strongest crustal shear wave anisotropies, up to 20%, have been reported in recent orogenic belts, such as the Himalayas (e.g., Xie *et al.*, 2013) or the Andean Cordillera (Lynner *et al.*, 2018). Nonetheless, high RAs (10-16%) have also
50 been in many other parts of the world with very different tectonic histories, even in sedimentary basins (Dreiling *et al.*, 2018), ancient orogenic belts (Wang *et al.*, 2020) or areas with intra-plate volcanism (Ojo *et al.*, 2017). Besides, lateral variations in the crustal anisotropy have been related to a wide catalogue of geological features: microcracks and metamorphic foliations (Guo *et al.* 2012), fault systems (e.g. Shirzad and Shomali, 2014; Shirzad, *et al.*, 2017), geological boundaries (e.g., Naghavi *et al.*, 2018; Wang *et al.*, 2020) or lateral crustal flow (e.g. Lynner *et al.*, 2018).

55 In this work, the first 3D crustal radial anisotropy model of NW Iberia is derived from the inversion of surface wave group velocities obtained from ambient noise interferometry (ANI) (e.g., Wapenaar, 2003, 2004; Shapiro and Campillo, 2004; Snieder, 2004). This area (Fig. 1a) is a geologically complex region with a long and well-established tectonic history that comprises the overlapping structural imprint of two major compressional events: the Variscan orogeny, in the Late Paleozoic; and the Alpine orogeny, in Cenozoic times, separated by several rifting episodes in the Mesozoic. The structure of
60 the study area was mainly configured during the Variscan orogeny, although the Alpine compression reworked some of the structures and originated a widespread pervasive fracturing, particularly in the upper crust. Overall, the part of the Variscan belt that crops out in the Cantabrian Mountains (CM) represents one of the most complete sections of this orogen in Europe, illustrating the transition from the internal zones of an orogenic system, in the West, to the external zone, to the East (Fig. 1b). From the early 90’s, extensive deep seismic reflection and refraction/wide angle surveys were carried out in the area.



65 These programs focused in the unveiling of the deep crustal structure of the CM (Pérez-Estaún *et al.*, 1994; Pulgar *et al.*,
1995, 1996; Álvarez-Marrón *et al.*, 1996, 1997; Gallastegui *et al.*, 1997, 2002; Ayarza *et al.*, 1998; Fernández-Viejo *et al.*,
1998, 2000; Fernández-Viejo and Gallastegui, 2005; Fernández-Viejo *et al.*, 2011 2012) and helped to broaden the
knowledge about the multiorogenic crustal architecture. In order to increase the resolution in the structure of the crust,
several temporary seismic arrays with different specifications and dimensions were deployed in the CM (e.g. López-
70 Fernández *et al.*, 2012; 2018), the most recent of which is featured for the first time in this study.

Unlike active seismic methods, which can provide direct signals from faults or other discontinuities, the ANI reflects the
variation of the seismic velocities of the bulk rock, which is controlled by their elastic parameters. In orogenic belts, where
lithologies with different properties are placed in contact by structural features, ANI can also help to infer indirectly the
presence of structures at depth and thus it can be valuable for the unravelling of the upper crustal structure at regional or
75 even local scale (e.g Acevedo *et al.*, 2019; Sammarco *et al.*, 2017; Gu *et al.*, 2019; Green *et al.*, 2017; Olivar *et al.*, 2020).
Up to the date, there is limited knowledge on the seismic anisotropy signature of NW Iberia. Díaz *et al.* (2002, 2006, 2015)
studied the upper mantle and lower crust anisotropy from distant earthquake shear wave splitting measurements and
Acevedo *et al.* (2020) used local earthquake shear wave splitting and ANI analysis to infer the anisotropic properties of the
upper crust in the central part of the CM. Both studies consistently reported an average E-W fast direction, but the rotation of
80 the fast orientations in the vicinity of major Alpine structures suggest that the contribution of the Alpine deformation to the
anisotropy can be significant (Acevedo *et al.*, 2020).

Here we make use of the ambient noise recordings from a new temporary seismic network in NW Iberia to extend to the
North and the West an earlier tomographic S-wave velocity model of the eastern sector of the CM (Acevedo *et al.*, 2019),
which was mostly affected by the Alpine deformation, and to further determine the 3-D distribution of the crustal radial
anisotropy. From a subsequent work (Acevedo *et al.*, 2020), we learnt that the crustal fabric controlled the orientation of
85 fastest seismic velocities, sometimes in accordance with Variscan structures, others with Alpine structures. However, there
was coincidence in the orientation of Variscan and Alpine structures, mostly by reworking during the youngest convergence.
The aim of the new seismic array was two-fold, building on our previous experience. Firstly, to apply the ANI method to
learn differences in architecture in relation to two orogenic events with contrasting kinematics (therefore orientation of
90 structures). For this reason, we extended the area of observations to include parts of the Iberian crust with stronger Variscan
imprint, incorporating domains with strong tectonic fabric susceptible to produce seismic anisotropy (Cárdenes *et al.*, 2021)
and with contrasting orientation to Alpine structures (Figs. 1a and b). Secondly, to constrain in the upper crust the
contribution to seismic anisotropy by internally deformed rocks versus tectonically fractured rocks.



2 Geological setting

95 2.1 Tectonic history

The crustal architecture of the study area is mainly defined by the Variscan orogeny, which affected the continental crust of western Europe and the northwest of Africa between the Late Devonian and the Early Permian (e.g. Matte *et al.*, 1986; Ribeiro *et al.*, 2007; Martínez-Catalán *et al.*, 2009; Pastor-Galán *et al.*, 2013). Subsequently to the denudation of the Variscan orogen, several rifting episodes affected the crust in NW Iberia, first in the Permian-Triassic, then in the Mesozoic
100 where the crust was completely dismembered with the final opening of the Atlantic. The most important episode occurred between the Late Jurassic and the early Cretaceous and was related to the opening of the Bay of Biscay (e.g. Cadenas *et al.*, 2018; Tugend *et al.*, 2015). This event configured the crustal structure of the eastern part of the study area, beyond the Ventaniella fault (Fig. 1a).

In Cenozoic times, the dominant geodynamic regime of the region shifted again and caused the North-South
105 convergence between Europe and Africa, producing the onset of the Alpine orogeny. The compression started along the northern edge of the Iberian Peninsula in the Pyrenees and migrated to the West to form the CM (e.g. Teixell *et al.*, 2018). During the convergence, the transitional crust of the Bay of Biscay was underthrust southwards beneath the Iberian continental crust (e.g. Boillot *et al.*, 1979; Fernández-Viejo *et al.*, 2012; Cadenas and Fernández-Viejo; 2017). The bulk of the deformation was mainly accommodated by East-West oriented reverse faults and thrusts, but there are numerous
110 examples of the reworking and retightening of favourably oriented earlier Variscan thrusts and folds, with a different degree of development across the study area (e.g. Alonso *et al.*, 1996). Currently, in the North Iberian crust, Alpine structures are dominant in the eastern half of the Variscan foreland-fold and thrust-belt, but they decrease their importance towards the West (Alonso *et al.*, 1996; Martín-González *et al.*, 2012; Llana-Fúnez and López-Fernández, 2015).

2.2 Crustal structure

115 Numerous works have contributed to broaden the knowledge about the Variscan imprint in the crust prior to the rise of the CM (e.g. Julivert, 1971; Pérez-Estaún *et al.*, 1988; Alonso *et al.*, 2009) and, more recently, its evolution during the Alpine convergence (Alonso *et al.*, 1996; Pulgar *et al.*, 1996, 1999; Gallastegui *et al.*, 2002, Martín-González *et al.*, 2012; Pedreira *et al.*, 2015). From the early 90's, extensive seismic surveys were carried out in the area. These programs focused in the unveiling of the deep crustal structure of the CM from deep seismic reflection and refraction/wide angle data (Pérez-
120 Estaún *et al.*, 1994; Pulgar *et al.*, 1995, 1996; Álvarez-Marrón *et al.*, 1996, 1997; Gallastegui *et al.*, 1997; Ayarza *et al.*, 1998; Fernández-Viejo *et al.*, 1998, 2000; Gallastegui *et al.*, 2002; Fernández-Viejo and Gallastegui, 2005; Fernández-Viejo *et al.*, 2011, 2012) and led to significant findings that improved decisively the geological and geodynamical models of the area. For example, the E-W oriented profiles ESCIN-1 and ESCIN-3 imaged for the first time the Variscan structures of the crust under the CM and their progressive loss of importance compared to the Alpine structures towards the East. Later, the
125 ESCIN-2 profile was performed with the goal of sampling the Alpine features in the transition between the eastern sector of



the CM and the Cenozoic Duero basin. Both profiles revealed the presence of an important crustal root beneath the CM. In order to complement the active geophysical surveys, several temporary seismic arrays with different specifications and coverage were deployed in the CM. Besides the seismotectonic characterization of the region (e.g. Llana-Fúnez and López-Fernández, 2015; López-Fernández *et al.*, 2012; 2018) the recorded passive seismic data allowed the study of the crustal configuration of North Iberia using receiver function analysis (Díaz *et al.*, 2003, 2009a, Mancilla and Díaz, 2015) and validated many of the ESCIN observations. The use of ambient noise interferometry is also beginning to provide knowledge about the structure of the upper crust in the study area (e.g. Acevedo *et al.*, 2019, 2020; Olivar *et al.*, 2020).

2.3 Upper crustal domains in the study area

In the central sector of the CM the erosion of the Mesozoic sedimentary cover during the mountain building led to the exposure of the underlying Paleozoic basement. Overall, the part of the Variscan Belt that crops out in the CM represents one of the most complete sections of this orogen in Europe, illustrating the transition from the internal zones of an orogenic system, in the West, to the external ones, to the East. The physical properties of large parts of the upper crust targeted in this study with ambient noise tomography can be predefined according to the nature of the rocks and the structures, based on surface geology. As it has already been mentioned, a major part of the crustal architecture was shaped during the development of the Variscan orogeny and for that reason, the crustal domains that will be defined below follow partially the subdivision established for the Variscan orogeny (Julivert *et al.*, 1971). However, subsequent tectonic events, although did not produce a significant change in the nature of rocks, did have an impact on their structure. In most cases, producing a tendency to upright structures by increasing the dip of cartographic units and structures (e.g. Alonso, 1989).

The first crustal domain to the East of the study area is the foreland-fold-and-thrust belt of the Variscan orogen, the external part of the orogenic belt, corresponding to the Cantabrian Zone (CZ) in the literature (e.g. Alonso *et al.*, 2009). It is composed by sedimentary rocks that bear no tectonic or any other type of fabric orienting rock-forming minerals. However, the arrangement of tectonic units during the Variscan orogeny led in the final stages of the orogeny to the upright attitude of thrust sheets (e.g. Merino-Tomé *et al.*, 2009). Folding of syn-orogenic sediments not involved in earlier Variscan thrusting also led to the upright position of lithostratigraphic units (e.g. Alonso y Pulgar, 1989; Aller and Gallastegui, 1995).

To the West of the Variscan foreland-fold-and-thrust belt in the basement lies the hinterland of the orogen, showing an approximate N-S arrangement in the study area (Fig. 1a). In terms of the rock types, their fabric, and their attitude we could distinguish four domains: a linear slate belt wrapping around the external part of the Variscan orogen, a subhorizontal slate belt coinciding partly with the Mondoñedo nappe (Bastida *et al.*, 1986), a subvertical high grade metamorphic domain pervasively intruded by Variscan granitoids, and the allochthonous nappes of high-grade rocks sitting on top of the previous domain.

The linear slate belt is a domain that can be defined ahead of the Mondoñedo nappe, over the Navia-Alto Sil domain (Marcos, 1973). From the structural point of view, most of the structures are steeply dipping (Marcos, 1973) and they coincide with an area with a N-S lineation fabric (Matte, 1968). The rocks present a tectonic fabric developed at low-grade



160 metamorphic conditions, which imposes a strong mostly planar mechanical anisotropy to the propagation of seismic waves
(Cárdenes *et al.*, 2021).

The subhorizontal slate belt coincides with the mid and rear part of the Mondoñedo nappe (Fig. 1). The overall structure
in the upper crust, as deep as 10 km in current crust, is dominated by the presence of large recumbent folds (Matte, 1968;
Bastida *et al.*, 1986). This isoclinal folding is accompanied by a tectonic fabric equilibrated in medium to high grade
conditions that strengthens the subhorizontal anisotropy imposed by the orientation of the layers. Altogether, the linear and
165 the subhorizontal slate belts constitute the West-Asturian Leonese Zone (WALZ).

The high-grade domain West of the Vivero fault (Fig. 1a) corresponds to the Central-Iberian Zone (CIZ). It is
constituted by a rock sequence similar to that of the WALZ, but at higher grade given the pervasive intrusion of Variscan
granitoids throughout the history of the orogenic belt over millions of years. The recognition of large recumbent folds is
hindered by the large amount of granitoids, exceeding 50 % of current exposure locally, and by the development of
170 subvertical structures in the late stages of the Variscan orogen, mostly upright folds and subvertical shear zones (e.g. Llana-
Fúnez and Marcos, 2007). The folding is accompanied in several locations by the development of a locally strong
crenulation fabric (e.g. Bastida *et al.*, 2010). Subvertical corridors of foliated rocks in relation to large shear zones are
common and often affect several kilometres on either side of the crustal scale structures (e.g. Llana-Fúnez and Marcos,
2001).

175 The last domain corresponds to the allochthonous nappes, which are thrust sheets of exotic provenance thrust over the
CIZ (e.g. Martínez-Catalán *et al.*, 1997). The presence of these allochthonous complexes defines the Galicia-Trás-os-Montes
Zone (GTOMZ). Several units have been differentiated within them, the essential features are that are mostly made of high-
grade high-pressure rocks, bearing a strong tectonic fabric and showing a subhorizontal attitude (see e.g. Marcos *et al.*, 2002
for Cabo Ortegal complex and Martínez Catalán, *et al.*, 2012 for the Órdenes complex). Geological sections based on surface
180 geology show that they extend several kilometres at depth in the current continental crust.

The upper crustal domains presented have been defined by the types of rocks and structures formed during the Variscan
orogeny. Subsequent tectonic events in the study area lack the intensity and the pervasive character shown during the
Variscan orogeny. No tectonic fabric at regional scale has been reported in relation to either the several extensional episodes
leading to the opening of the Atlantic neither during the more recent Alpine convergence. Faults are also more spaced in
185 between.

It is only in the first of the domains defined, in the CZ, that it has been reported a somehow widespread effect of Alpine
deformation over previous rocks and structures, dominated by the tightening of previously steep Variscan structures (e.g.
Alonso and Pulgar, 1989). Locally in this domain, there are reports of evidence of post-Variscan fracturing. Although no
systematic study of Alpine fracturing has been carried out in the study area, however, separate observations in post-Permian
190 rocks in the confines of the CZ show the development of subvertical N-S set of joints (e.g. Lepvrier and Martínez García,
1990; Pastor-Galán *et al.*, 2011; Uzkeda *et al.*, 2013).



3 Data and methods

3.1 Seismic data

This study used continuous broadband seismic data from 13 portable seismic stations located in the western CM. 11
195 stations were deployed in the framework of the Geocantábrica-Costa (Geocantábrica-Costa Seismic Network, GEOCSN)
experiment, while the other two stations belong to the permanent Spanish Seismological Network (SSN) of the Spanish
Geographical Institute (Fig. 2a). The seismic array served the dual purpose of enhancing the location of the intraplate
seismicity in the West of the CM and the close continental shelf and acquiring new passive data for ambient noise analysis.
The experiment covered an area of $\sim 12,500 \text{ km}^2$ with interstation distances of $\sim 40 \text{ km}$. Seismic stations were equipped with
200 Nanometrics Taurus data loggers and broad-band Trillium 120 s sensors recording 3-component seismic data at a sample
rate of 100 Hz. Most of the stations were installed in isolated chapels and sheds with connection to the electricity network,
although solar power supply was required in some locations. A few stations were also mounted directly in the field, buried in
 $\sim 0.5 \text{ m}$ pits. The network operated for 9 months between June 2019 and February 2020 with an average data recovery of
96% due to occasional power cuts caused by thunderstorms. To extend our observations to the West, we also processed a
205 year of continuous seismic data registered by 7 stations of the northern IberArray deployment (Díaz *et al.*, 2009b) plus the
station EPON of the SSN (Fig. 2a). The seismic recording equipment and their technical configuration were the same as in
the GEOCSN, except that all the seismic stations were mounted outdoors. The station spacing was also larger, around 60 km,
covering an area of $\sim 10,000 \text{ km}^2$ with a 26% of overlap with the GEOCSN.

3.2 Ambient noise interferometry

210 The treatment of the seismic ambient noise data to obtain Rayleigh- and Love-wave dispersion velocities was based on
the widely used processing scheme described by Bensen *et al.* (2007), with a few modifications. Our processing began with
the splitting of the continuous dataset in 24-hour long segments and the removal of all the traces with gaps. The records were
downsampled to 25 Hz and the instrument responses were removed. Next, the mean and the trend were also removed from
the traces and a band-pass filter with corner frequencies between 0.01-2.0 Hz was applied. The described pre-processing
215 benefited from the use of the Phase Cross-Correlation technique (PCC, Schimmel, 1999) for the calculation of the cross
correlations. Given that PCC is amplitude unbiased (Schimmel *et al.*, 2011), we did not perform any temporal or spectral
normalization, thus avoiding the potential introduction of artifacts and shortening the processing time. The next step
consisted in the cross correlation of the 24-hour traces recorded simultaneously by each pair of stations with the
aforementioned PCC procedure. In this way, we obtained the Daily Cross-Correlation Functions (DCCF) for lag times of
220 100 s. The observation of the cross-correlograms revealed a noticeable asymmetry between the causal and the acausal parts
of the signal. Since we ignore which of these parts contain more useful information, the causal and the time reversed acausal
parts of each station-pair DCCF were stacked using the Time-Frequency domain Phase-Weighted (tf-PWS) procedure of
Schimmel and Gallart (2007). This stacking method enhances the coherent signal and cancels incoherent noise, allowing the



225 extraction of the symmetrical empirical Green's functions (EGF) of the medium between each station pair. In this study, we processed the vertical (Z) and the horizontal components (E, N) to obtain the Z-Z (Fig. 3a), E-E and N-N EGFs. Then, the horizontal components were rotated along the azimuth of the interstation path to provide the radial (R-R, Fig. 3b) and transverse (T-T, Fig. 3c) correlation functions. The vertical and the radial components are dominated by Rayleigh waves (Figs. 2a and 2b), whereas Love waves emerged from the transverse component (Figs. 2a and 2c).

230 The measurement of the Rayleigh and Love group velocity dispersion curves was performed by using the multiple filter analysis method (MFA) of Dziewonski *et al.* (1969). In this technique, a narrow-band Gaussian filter is applied over different periods to isolate the wave package around the central period of each filter (Fig. 2d). The group velocities in their fundamental mode were then manually picked to construct dispersion curves. According to Bensen *et al.* (2007), dispersion curves are limited at the longer periods by the fact that velocity measurements are only reliable for interstation distances greater than three wavelengths. Given the dimensions of our network, the strict compliance of this criterion results in a loss
235 of measurements that affects the resolution of the group velocity maps at periods > 10 s. However, Luo *et al.* (2015) demonstrated that consistent measurements can also be obtained using a cut-off of one wavelength.

In order to avoid discarding useful data without relaxing the constraints to a point at which the velocity determinations become unreliable, we adopted a two-wavelength criterion in this work. This cut-off has been proven to be a suitable compromise solution in other studies (e.g. Sammarco *et al.*, 2017; Brandmayr *et al.*, 2016, Shapiro *et al.*, 2005). To ensure
240 the quality of the results, our analysis was limited to velocity measurements within two standard deviations from the mean and with more than 60 measurements at each period. The stability of the dispersion curves was also investigated by stacking sets of 30, 60, 90 and the available DCCFs for all the interstation paths (Fig. S1). Overall, Love wave dispersion curves are slightly less stable than Rayleigh wave dispersion measurements. Waveforms and dispersion curves for the GEOCSN paths stabilize at a lower number of days (~ 60 days) than IberArray paths (~ 90 days) but, in both cases, the stabilization is reached
245 at a much lower number of days than the available for each interstation path (Fig. S1). We decided not to extract phase velocities due to the difficulty of resolving the 2- π phase ambiguity without long period data, due to the small aperture of our seismic network and the complexity of the CM crust. Thus, the estimation of the velocity uncertainties is vital to warrant the trustworthiness of the results. For this task, we have checked the group velocity mismatch between the dispersion curves obtained from 10 stacks made with the randomly selected 75% of all the available DCCF (Fig. S1). The results show, in
250 general, uncertainties well below 1% for the Rayleigh and Love wave group velocity determinations. In relative terms, Love waves display higher velocity uncertainties than Rayleigh waves, so as the IberArray dataset when compared with the GEOCSN measurements.

3.2 Group velocity tomography and depth inversion

Reliable dispersion measurements of Rayleigh and Love waves were obtained at periods between 2-14 s (Figs. 2e and
255 2f). The transformation of the dispersion velocities between the stations into continuous Rayleigh and Love group velocity surfaces was performed with the Fast-Marching Surface Tomography scheme (Rawlinson, 2005). The FMST is an iterative



non-linear method that is implemented in two steps: a) the forward prediction of travel-times with the fast-marching method (Sethian, 1996; Rawlinson and Sambridge, 2004a; Rawlinson and Sambridge, 2004b) and b) the modification of the model parameters to explain the data observations, for which a subspace inversion scheme is used (Kennett *et al.*, 1988). The resulting models are controlled by a grid of nodes with cubic B-spline interpolation that generates a smooth and continuous velocity medium. We selected a grid size of $0.1^\circ \times 0.1^\circ$ for the inversion of a homogeneous starting model that was created from the average velocity measured for a certain period (Nicolson *et al.*, 2014). After extensive tests, the smoothing and damping parameters were set to 0.001 and 0.1, respectively, but their change only had a minor influence in the resulting models.

Based on the set of tomographic group velocity maps, we created new pseudo-dispersion curves by extracting the Rayleigh and Love velocity values for each point of a $0.1^\circ \times 0.1^\circ$ grid. The independent inversion of these curves with the CPS surface inversion codes (Herrmann, 2013) allowed us to reconstruct the variation of the V_{sv} and the V_{sh} with depth in each grid node. In order to address the non-uniqueness nature of the inversions, we calculated two initial regional S-wave velocity model to be used as input in each of the subsequent computations. These models were obtained in a previous step from the separate inversion of the average Rayleigh and Love dispersion curves in the whole study area (Figs. 2e and 2f). We started in all cases from a homogeneous 22-layer model, the first four layers with a thickness of 0.5 km and the rest with a thickness of 1 km. Based on published studies in the area (Fernández-Viejo *et al.*, 2000), we defined a constant S-wave velocity of 3.35 km/s, with a fixed V_p/V_s ratio of 1.74 and a density of 2,600 kg/m³. The mismatch between the S-wave estimations from Rayleigh and Love waves allowed us to assess the intensity and distribution of the RA following Eq. (1):

$$RA(\%) = \frac{2(V_{sh} - V_{sv})}{(V_{sh} + V_{sv})} 100, \quad (1)$$

(Yanovskaya *et al.*, 1998; Savage, 1998; Ojo *et al.*, 2017). All the inversions were performed with a damping factor of 10 in the first iterations to avoid an excessive shift from the initial model, whereas a value of 0.5 was used for the remaining iterations.

4 Results

4.1 Rayleigh and Love wave group velocities

In total, we extracted Rayleigh and Love dispersion measurements of 78 station pairs from the GEOCSN network and 28 additional station pairs from the IberArray network. The 2-D tomographic maps displaying examples at selected periods of Rayleigh and Love group velocity variations can be observed in Fig. 4. Considering the Rayleigh waves (Fig. 4, left panels), the absolute group velocities range between 2.3 and 3.1 km/s. On the other hand, Love waves (Fig. 4, right panels) show slightly faster velocities, varying between 2.3 and 3.4 km/s. At all periods, both Rayleigh and Love derived maps image two clear blocks: a high velocity zone occupying the western half of the study area and a relative low velocity zone in the eastern half. Both anomalies are separated by a narrow C-shaped transition sector which follows the boundary between



the CZ and the WALZ and the surface trace of the main structures. The western anomaly presents high and moderately stable group velocities in the entire period range. On the contrary, group velocities in the eastern anomaly zone raise constantly as the period increases. The most noticeable difference between Rayleigh and Love maps lies in the shape of the western anomaly at the highest periods. At those periods, Rayleigh group velocities display a light decrease, and the high velocities tend to concentrate in the South. However, Love group velocities keep delineating a large high velocity surface in the western sector, while the low velocity anomaly migrates towards the South.

The resolution of the final velocity slices was investigated by performing synthetic checkerboard tests (Figs. S2 and S3). We used as reference three models with small (20 x 20 km), medium (30 x 30 km) and large (40 x 40 km) anomaly sizes and velocity perturbations of ± 0.4 km/s. Then, we evaluated the performance of our array for recovering this previously known velocity structure at periods of 4, 8 and 12 s. For both Rayleigh and Love waves, at periods up to 8 s, the resolution is sufficient to resolve anomalies of ~ 20 km, in the central and eastern sectors of the study area, and ~ 30 km in the westernmost zone. At periods longer than 8 s, the resolution decays due to the progressive decrease of the number of interstation paths and signs of smearing arise in the models. The average size of the recovered features increases to ~ 30 km. At those long periods, the Rayleigh paths recovered more accurate models than the Love paths. The RMS misfit between observed and predicted travel times ranged between 0.3-0.8 s, and 0.7-1.2 s for the Rayleigh and Love waves respectively, which indicates that the inverted models fit the observations and they are not affected by the selection of the regularization parameters (Nicolson *et al.*, 2012).

4.2 Shear wave velocities

Figure 5 shows examples of the S-wave inversion results in specific grid points located in the CZ (Fig. 5a), the WALZ (Fig. 5b) and the CIZ+GTOMZ (Fig. 5c), featuring a good fit between the observed and the inverted data. The models and the anisotropy characteristics from the WALZ and the CIZ+GTOMZ show similar patterns, whereas the CZ presents some peculiarities, such as a constantly increasing V_{sv} and V_{sh} velocity with depth and a pronounced negative radial anisotropy anomaly near the surface. Figure 6 shows examples of the variation of V_{sv} (Fig. 6, left panels) and V_{sh} (Fig. 6, right panels) at depths of 3, 6, 9 and 12 km. Within that depth range, the average V_{sv} increases from 3.0 to 3.4 km/s, while average V_{sh} oscillates between 3.1 and 3.5 km/s. Similarly to the group velocity maps, the presence of a low velocity anomaly to the East of the study area stands out both in V_{sv} and V_{sh} maps and its limit runs parallel to the curved boundary between the external and the internal zones, between the CZ and the WALZ. However, this anomaly attenuates at depth and finally disappears below ~ 6 km. At higher depths (>9 km) the correspondence between the features depicted in the V_{sv} and the V_{sh} maps begins to fade away. In the V_{sv} surfaces, two new high velocity anomalies emerge in the South. However, the V_{sh} maps depict high velocities in the western/central sector and in the northeastern corner.



4.3 Radial anisotropy

The spatial distribution of the radial anisotropy (Fig. 7) was calculated from the discrepancies between V_{sv} and V_{sh} in each node of the tomographic grid (Figs. 5a, 5b and 5c). In absolute values, the whole study area shows a significant anisotropy that reaches 10-15% in certain areas. Nevertheless, there is a clear differentiation with depth. At depths shallower than ~8 km the anisotropy strength keeps within the $\pm 6\%$ range. Beneath those depths, the anisotropy starts to rise up to ~15%. In terms of the anisotropy style, negative anomalies ($V_{sv} > V_{sh}$) are dominant at shallow depths in the eastern half and the southwestern limit of the study area, with a weak positive corridor separating them. As greater depths, the negative anomalies become positive ($V_{sv} < V_{sh}$) at ~6 km and ~8 km, respectively.

In order to represent the velocity variations within the context of the Variscan structure of the CM, we constructed an E-W cross section that runs perpendicularly to the main Variscan elements (Fig. 8). The most striking feature of the V_{sv} (Fig. 8a) and the V_{sh} (Fig. 8b) cross sections is the low velocity anomaly located in the East. The V_{sh} section shows a more extensive anomaly that coincides with the CZ. In the case of the V_{sv} section, the anomaly is more localized towards the sector where the syn-orogenic deposits of the Central Coal basin (CCB) are present. The previous S-wave tomography in Acevedo *et al.*, 2019 allowed us to extend the V_{sv} section until the transition between the CZ and the Basque Cantabrian basin (BCB). The higher velocities in both sections show a good correlation with the expected distribution of the Precambrian basement. In general, the internal zones show a more homogeneous velocity pattern, although V_{sv} is quite constant and V_{sh} depicts a velocity increase with depth. The latter type of waves also register a slight reduction of velocity in the GTOMZ and CIZ domains in comparison with the WALZ. The anisotropy E-W section (Figures 8c and 9) also shows a strong correlation with the main geological domains (Figs. 1 and 8c). The mentioned positive corridor roughly coincides with the WALZ, while the negative patches are limited by the Vivero fault, that marks the beginning of the CIZ, and the Narcea antiform. To the East of the latter structure, the negative anisotropy is only observed in the part of the CZ where syn-orogenic deposits are absent. On the other hand, the high positive anisotropies are roughly consistent with the presence of the lower Paleozoic and Precambrian basement rocks at depth.

5 Discussion

Tomographic maps in Figure 6 depict the first high-resolution S-wave models of the transition between the internal and the external parts of the Variscan orogen in NW Iberia. Considering the sensitivity of the method (Fig. S4), the discussion of the results is restricted to the first 12 km of the crust. In addition, at the investigated periods (<14s) Love waves are primarily sensitive to the uppermost crust, while the sensitivity peak of Rayleigh waves deepens as the period increases. The following discussions are only focused on well-resolved areas from the checkerboard tests (Figs. S2 and S3).



5.1 Velocity structure in the upper crust

In previous ambient noise regional studies on the Iberian Peninsula, Macquet *et al.* (2014) and Palomeras *et al.* (2017) reported S-wave velocity values at 5 km depths ranging between 2.5 km/s and 3.5 km/s in the study area. Likewise, a recent
350 work centered in the BCB also obtained this velocity range for the upper crust in the eastern termination of the CZ (Olivar *et al.*, 2020). Silveira (2013) and Palomeras (2017) identified a first order anomaly which corresponds with the Iberian Massif and recognized some of the tectonic units that constitute it. However, due to resolution limitations, the transition between the internal and external zones was poorly constrained. In contrast, the most striking element of our models, both the surface- and the shear-wave ones, is the precise delineation of the boundary between these domains by a sharp velocity change (Figs.
355 4 and 6).

The contour of this limit depicts a clear convex-to-the-west shape with the CZ located at its core. The contact between the high velocity anomaly, to the West, and the low velocity anomaly, to the East, is parallel to the Narcea antiform (NA), which is the structure that marks the boundary between the hinterland and the external zones of the Variscan orogen (Fig. 1) (Gutiérrez-Alonso, 1992; Pérez-Estaún *et al.*, 1994). The presence of rocks with completely different physical properties at
360 both sides of the eastern boundary of the NA justifies the observed velocity contrast. The CZ is constituted by a sedimentary sequence that forms the foreland fold and thrust belt of the Variscan orogen, in a thin-skinned deformation context. On the other hand, the slate belt to the West, is a relatively homogeneous domain mainly composed by siliciclastic rocks affected by a low grade of metamorphism. In summary, the upper crust in the CZ is essentially made of sedimentary rocks without metamorphism while the upper crust in the NA and the WALZ slate belt is composed by igneous and volcanic rocks in the
365 NA and low grade metamorphics towards the West, generating a clear contrast in physical properties as reflected in the velocity patterns.

The sedimentary rocks of the CZ display relatively low S-wave velocities, typically under 3.0 km/s in the V_{sv} models or 3.2 km/s in the V_{sh} estimations. The profile of Figure 8a display a good correspondence between the lower velocities and the location of the siliciclastic wedges of syn-orogenic sediments. In fact, the low velocity anomaly reaches its greater thickness,
370 around 5 km, in the CCB, the largest of these wedges. The depth estimation in the CCB is consistent with previous interpretations (Aller and Gallastegui, 1995). Towards the West, both the V_{sv} and the V_{sh} models depict high velocities. V_{sv} remain constant about 3.3 km/s, while V_{sh} increases steadily with depth (Fig. 6). The rock sequences in the WALZ are quite homogeneous, although in the cross-section of Fig. 8a some high velocity patches can be identified between 5-9 km depth. The anomaly located close to the orogenic boundary is related with the stack and thrusting of rigid lower Paleozoic and pre-
375 Variscan basement rocks from the NA (Pérez-Estaún *et al.*, 1994) and the exhumation of basement rocks, gneiss and pre-Variscan igneous rocks between the NA and the Allande fault (Marcos y Pulgar, 1982; Rubio-Ordóñez *et al.*, 2015). A smaller high velocity anomaly, in the West, is located near the Vivero fault (Fig. 8a) (López-Sánchez *et al.*, 2015). High velocities were expected in this area due to the presence of mafic rocks and Variscan granitoids. However, the V_{sh} profile (Fig. 8b) registers a velocity reduction in this domain, maybe caused by the fact that the resolution in the edges of the models



380 decays and velocities are less well constrained. The basement rocks at the surface also show pervasive fracturing and weathering, strongly affecting velocities.

5.2 Thickness of the sedimentary layer and basement depth

A significant result from S-wave models is the estimation of the thickness of the sedimentary layer. In Macquet *et al.* (2014), a S-wave velocity value of 2.9 km/s is proposed to indicate the limit between the basement and the sedimentary cover. In our case, this velocity defines quite well the position of the syn-orogenic sequence in the CZ, the presence of small Permo-Triassic basins in the CZ - BCB transition and the presence of Mesozoic sediments in the BCB but fails in recovering the depth of the basement. The main detachment of the CZ is believed to be located near the Precambrian-Cambrian boundary (Pérez-Estaún *et al.*, 1988). Taking into account that the pre-Variscan basement rocks are exposed in the NA and show velocities around 3.1 km/s in Figure 8a, we considered that this can be a more appropriate value to estimate the depth of the basement-cover surface in our study area and infer the position of the detachment. The 3.1 km/s iso-velocity line initiates in the NA area. It stretches towards the East for 20 km at shallow depths and then it sinks almost vertically until reaching 8 km. This deepening coincides with the maximum eastern extension of the pre-Variscan rocks at depth. Continuing to the East, the surface dips smoothly to the West and alternates ramps and flats until reaching depths of 1 km to the West of the Ventaniella fault. In the extension of Fig. 8a, based on the V_{sv} model of Acevedo *et al.* (2019), the iso-velocity line deepens again, showing an apparent dip towards the East. This change is related with the different structure of the CZ-BCB transition, which was mainly configured by the Alpine inversion of Mesozoic extensional faults (e.g. Espina, 1997; Tavani *et al.*, 2011). If we consider that the 3.1 km/s surface depicts the location of the base detachment of the CZ, its greatest depth ranges around 8-9 km. This observation agrees with the studies of Pérez-Estaún *et al.* (1988; 1991; 1994), although it is slightly shallower than the estimations of Gallastegui *et al.* (1997, 2000).

400 5.3 Radial anisotropy

From the relation between V_{sv} and V_{sh} in Eq. 1 we have obtained the first model of RA in the continental crust in NW Iberia (Figs. 7, 8c and 9). Overall, the RA patterns display a fair correspondence with the main Variscan tectonic units, at least in the shallowest crust (<7 km). At those depths, the distribution of the RA negative anomalies bound the GTOMZ-CIZ and the CZ, whereas in the WALZ a constant positive anisotropy is observed (Fig 8c). The RA style is related with the inclination of the anisotropic features (Dreiling *et al.*, 2018, Xie *et al.*, 2013). Thereby a negative RA implies the presence of steeply dipping to subvertical structures (60-90°) while a positive RA suggest gently dipping to horizontal features (0-30°). Thus, in the CZ, the negative anomaly can be explained by the verticalization of Variscan nappes and other structures, and the retightening of folds caused by the Alpine convergence, which was more intense in this domain than in any other. Moreover, the presence of a N-S oriented pervasive Alpine fracture system with subvertical dip has been recognized in the area and may play a significant role in the development of the anisotropy.



As the depth increases, the thrusts reduce their dip as they approach to their imbrication with the CZ basal detachment (Pérez-Estaún *et al.*, 1991), which is reflected in the progressive shift to a positive anomaly (Fig. 9). There are two factors that suggest that this change can be provoked by the presence of a basal detachment at those depths. First, the positive RA points towards the presence of smoothly dipping anisotropic features. Second, the RA style inversion occurs at shallower
415 depths beneath the CZ than the CIZ-GTOMZ, implying a possible structure with a general dip towards the West. Coherently, in the Eastern area of the CZ, the positive anomaly gets close to the surface. Laterally, RA style variations are also present, as in the transition between the CZ and the WALZ. From the Narcea antiform to the Mondoñedo thrust, subvertical structures are dominant, but the existence of an Alpine horizontal foliation parallel to the fold axis may compensate their effect and explain the slightly positive anomaly instead of the expected negative anisotropy. To the West of the MT, in the
420 internal zones of the orogen, the structures and foliation are mainly gently dipping. Despite that the CIZ and the GTOMZ are the less well constrained zones of our model, a negative RA anomaly is depicted up to 8 km depth. This observation contrasts with the subhorizontal structure in the rocks and units that characterize those domains. The anomaly can be justified by the presence at the surface of a strong subvertical deformation fabric related to late Variscan shear zones and folds (Llana-Fúnez and Marcos, 2007) or, more likely, by N-S fracture systems associated to the Alpine convergence.

In general, the magnitude of the RA is low, around 4%, at shallow depths (< 8 km). Considering the entire range of investigated depths, except for the WALZ, where the RA magnitude increases almost steadily, a progressive decrease followed by a rapid increment of the RA anisotropy magnitude is observed in the CZ and the CIZ/GTOMZ (Fig. 8c). A similar magnitude pattern was described in a previous study of the azimuthal anisotropy in the CM based on ambient noise interferometry (Acevedo *et al.*, 2020). In this work, a sharp decline of the anisotropy magnitude was reported at periods
430 between 4 and 7 s (~3 to ~6 km depth). At higher periods, the anisotropy rises again until it reaches magnitudes about 9% at 10 s, in agreement with our estimations. Nonetheless, the RA magnitudes at depths < 3 km yield greater discrepancies, as they are generally inferior to those obtained by azimuthal analysis.

At shallow depths (<5 – 10 km), the RA is believed to be caused by the alignment of stress- (Crampin, 1978; Crampin and Peacock, 2005) or structure-induced fluid saturated cracks (Zinke and Zoback, 2000). The fast anisotropic directions
435 obtained from shear-wave splitting in Acevedo *et al.* (2020) favor a structure-controlled anisotropy model for the CZ. What is more, although the Alpine deformation did not produce pervasive deformation in NW Iberia, it generated shallow fracture systems that can affect decisively the physical properties of the rocks near the surface, especially in the CZ and the CIZ/GTOMZ. Whatever the dominant mechanism is, the progressive closure of the open cracks due to the increment of the lithostatic pressure can explain the observed RA magnitude reduction at shallow depths. In crystalline low porosity rocks,
440 the complete closure of microcracks at grain boundaries is observed in laboratory experiments at about ~200 MPa, which is equivalent to depths around 8 km (e.g. Christensen, 1985; Guo *et al.*, 2014). In the case of slates from the WALZ, recent laboratory data have shown that the magnitude of the anisotropy increases with the decrease of confining pressure, as the orientation of the microcracks is strongly controlled by the shape fabric in very well foliated slates (Cárdenes *et al.*, 2021). However, this means that another origin must be invoked to produce the RA magnitude increment at higher depths. As it is



445 depicted in Fig. 1, the crystalline basement rock outcrops in the WALZ, showing an anisotropy that increases from 2% to
15% in depth. These Precambrian rocks, as well as the Lower-Paleozoic pre-Variscan siliciclastic sequences that form the
WALZ, are affected by low-grade metamorphism and the development of a widespread tectonic foliation. Anisotropic
minerals, such as phyllosilicates, are common in the composition of these rocks, so the alignment of minerals and grains
(Wenk *et al.*, 2020; Cárdenes *et al.*, 2021) seems to be the most likely mechanism controlling the anisotropy in the WALZ
450 and at depths > 8 km.

Many studies have tried to establish the linkage between tectonic regimes and RA patterns (e.g. Luo *et al.*, 2013;
Dreilling *et al.*, 2018; Wang *et al.*, 2020). Generally, compressional and extensional regimes are associated to the vertical
and horizontal alignment of cracks and minerals, respectively. However, the specific geodynamic setting of each location
must be considered, given that both regimes can produce very different anisotropy signatures. The presence of negative RA
455 at shallow depths in foreland fold-and-thrust belts has been observed in orogens worldwide. For example, Chen *et al.*, (2009)
and Guo *et al.*, (2012) reported negative RAs in the Himalayan fold-thrust belt. Recently, Wang *et al.* (2020) described a
widespread negative anomaly of ~5% below the Foreland belt of the Canadian Cordillera that turns into a positive anomaly
in the Omineca Belt, the hinterland of the orogen. These authors suggest that the RA in the foreland fold and thrust belts is
caused by the horizontal contraction of the upper crust, which creates subvertical faults and/or preferentially alignments of
460 minerals under convergent regimes. The continuity of the negative anomaly at depths up to 20 km allowed them to infer a
“thick-skinned” Cordillera-Craton transition. Contrarily, in our model, the negative anomaly in the CZ is distinctly limited at
depth (Fig. 9), pointing to a “thin-skinned” style of deformation, in accordance with previous studies (e.g. Pérez-Estaún *et al.*,
1994). On the other hand, positive anisotropy in the hinterland is usually associated to horizontally sheared fabrics,
which in the case of the Variscan orogen could either be caused during pervasive deformation associated to plate duplication
465 in convergence (e.g. Martínez-Catalán *et al.*, 1997), or by syn- or post-collisional localized crustal extension, as reported for
the Mondoñedo thrust (Marcos, 2013). Ductile crustal flow has also been invoked as the origin of positive RA anomalies,
mostly in the middle and lower crust (Lynner *et al.*, 2018), and this has also been suggested to occur at the late stages of the
Variscan orogeny for a significant part of the hinterland of the Variscan orogeny in NW Iberia (Llana-Fúnez and Marcos,
2007).

470 **6 Conclusions**

In this study, we used group velocity measurements from Rayleigh and Love waves to derive the first S-wave velocity
model of the continental crust in NW Iberia. The observed discrepancy between the measurements from Rayleigh and Love
waves impeded the possibility of performing a joint inversion of the dispersion curves and suggested the existence of crustal
radial anisotropy. Instead, an independent inversion of the Rayleigh and the Love group velocity estimations was done to
475 create a vertically polarized S-wave model and a horizontally polarized S-wave model, respectively. The first model
displayed velocities between 2.3 and 3.6 km/s, while the velocities of the latter ranged between 2.6 and 4.2 km/s. Both



models clearly depict the contrast in physical properties between the rocks located in the external (CZ) and the internal (WALZ, CIZ and GTOMZ) zones of the Iberian Variscan orogen, delineating the core of the large Western European Variscan belt: the core of the Ibero-Armorican arc at the Cantabrian Zone. Moreover, the high resolution of the models and the good geological knowledge of the area allowed us to associate the observed velocity changes to the variation of the bulk properties of the rocks caused by other first-order orogenic structures, such as the basal detachment of the CZ or the presence of a pre-Variscan basement in the NA, or sedimentary features such as the presence of syn-orogenic wedges in the CZ.

The crustal radial anisotropy 3-D model has been proved useful to identify and characterize the different terrains and units that form an orogenic belt and show a good correspondence with the dip of the main structures. The anisotropy pattern can also be associated to the deformation history of the orogen. A negative anomaly is found in the foreland fold-and-thrust belt, which can be related to the stack of thrusts and vertical fabrics caused by compression. In the internal areas, widespread positive anisotropy is accounted. The radial anisotropy magnitude oscillates between -4 and 15 % and increases with depth. Analyzing the depth pattern, we concluded that, at < 8 km depths, the alignment of Alpine fracture systems controls the anisotropy. At depths > 8 km, high and positive radial anisotropies are observed, caused by the presence of subhorizontal alignments of grains and minerals, possibly in relation with shearing in the basal detachment of the CZ and/or other shear zones formed during the development of the Variscan orogeny.

Code/Data availability

The datasets presented and used in this study were collected using a seismic network funded by project GEOCANTABRICA-COSTA (https://doi.org/10.7914/SN/YR_2019) and it can be released to the public on demand at GEOCANTABRICA@ftp.geol.uniovi.es. The deployment of the IberArray broadband seismic network (<https://doi.org/10.7914/SN/IB>) was part of the CONSOLIDER CSD2006-00041 (Geosciences in Iberia: Integrated studies on Topography and 4-D Evolution) grant from the Spanish Ministry of Science and Innovation. This dataset is available online at the ORFEUS Data Center (<http://www.orfeus-eu.org/>). Data processing used the open codes: Corr_stack_v04.1 (Schimmel et al., 2011) and Computer Programs in Seismology v3.30 (Herrmann, 2013). Figures were drafted using Generic Mapping Tools (Wessel and Smith, 1998) and QGIS 3.10.

Author contribution

J. A. is responsible for the deployment of the YR network, the processing of the seismic data and the redaction of the manuscript. G. F-V., S. L-F., C. L-F. and J. O. provided critical feedback and helped shape the research, analysis and manuscript. G. F-V., S. L-F and D. P-M. participated in the deployment and maintenance of the temporary experiment and the control of the data acquisition.



Competing interests

The authors declare that they have no conflict of interest.

Acknowledgments

This study was funded by research grants GEOCANTABRICA (GRUPIN14-044) and GEOCANTABRICA-COSTA
510 (GRUPIN18-000184). J.A. holds a PhD grant “Severo Ochoa” from the Asturias Government. (PA-17-PF-BP16139).
Additional support from grant CGL2017-86487-P is acknowledged. We thank the local people and institutions that helped to
install the seismic networks in Asturias, Galicia and León and the ICTJA-CSIC Seismic Laboratory
(<http://labsis.ictja.csic.es>) for sharing their seismic stations. We also thank the Instituto Geográfico Nacional (IGN, Spain)
for providing seismic data from the EARI and EPON permanent stations.

515 References

- Acevedo J., Fernández-Viejo, G., Llana-Fúnez, S., López-Fernández, C. and Olona, J.: Ambient noise tomography of the
southern sector of the Cantabrian Mountains, NW. Spain, *Geophys. J. Int.*, 219, 479-495, <https://doi.org/10.1093/gji/ggz308>,
2019.
- Acevedo, J., Fernández-viejo, G., Llana-Fúnez, S., López-Fernández, C. and Olona, J.: Upper crustal seismic anisotropy in
520 the Cantabrian Mountains (North Spain) from shear-wave splitting and ambient noise interferometry analysis, *Seismol. Res.
Lett.*, 92, 421-436, <https://doi.org/10.1785/0220200103>, 2020.
- Aller J. and Gallastegui, J.: Analysis of kilometric-scale superposed folding in the Central Coal Basin (Cantabrian zone, NW
Spain), *J. Struct. Geol.*, 17, 961-969, [https://doi.org/10.1016/0191-8141\(94\)00115-G](https://doi.org/10.1016/0191-8141(94)00115-G), 1995.
- Almqvist, B. S. and Mainprice, D.: Seismic properties and anisotropy of the continental crust: Predictions based on mineral
525 texture and rock microstructure, *Rev. Geophys.*, 55(2), 367-433, <https://doi.org/10.1002/2016RG000552>, 2017.
- Alonso, J. L., Marcos, A. and Suárez, A.: Paleogeographic inversion resulting from large out of sequence breaching thrusts:
The León Fault (Cantabrian Zone, NW Iberia). A new picture of the external Variscan Thrust Belt in the Ibero-Armorican
Arc, *Geol. Acta*, 7(4), 0451-473, <http://doi.org/10.1344/105.000001449>, 2009.
- Alonso, J. L. and Pulgar, J. A.: Síntesis cartográfica de la parte sudoccidental de la Zona Cantábrica, *Trabajos Geol.*, 18,
530 145-155, <https://doi.org/10.17811/tdg.18.1989.145-155>, 1989.
- Alonso, J. L., Pulgar, J. A., García-Ramos, J. C. and Barba, P.: Tertiary basins and Alpine tectonics in the Cantabrian 5
Mountains (NW Spain), in: *Tertiary basins of Spain: the stratigraphic record of crustal kinematics*, edited by: Friend, P. F.
and Dabrio, C. J., Cambridge University Press, Cambridge, UK, 214-227, <http://doi.org/10.1017/CBO9780511524851.031>,
1996.



- 535 Álvarez-Marrón, J., Pérez-Estaún, A., Danñobeitia, J. J., Pulgar, J. A., Martínez, J. R., Marcos, A., Bastida, F., Ayarza, P.,
Aller, J., González-Lodeiro, F., Banda, E., Comas, D. and Córdoba, D.: Seismic structure of the northern continental margin
of Spain from ESCIN deep seismic profiles, *Tectonophysics*, 264(1-4), 153-174, [https://doi.org/10.1016/S0040-1951\(96\)00124-2](https://doi.org/10.1016/S0040-1951(96)00124-2), 1996.
- Álvarez-Marrón, J., Rubio, E. and Torné, M.: Subduction-related structures in the North Iberian margin, *J. Geophys. Res.-*
540 *Sol. Ea.*, 102(B10), 22497-22511, <https://doi.org/10.1029/97JB01425>, 1997.
- Anderson, D. L.: Elastic wave propagation in layered anisotropic media, *J. Geophys. Res.*, 66(9), 2953-2963,
<https://doi.org/10.1029/JZ066i009p02953>, 1961.
- Ayarza, P., Catalán, J. R. M., Gallart, J., Pulgar, J. A. and Dañobeitia, J. J.: Estudio Sísmico de la Corteza Ibérica Norte 3.3:
A seismic image of the Variscan crust in the hinterland of the NW Iberian Massif, *Tectonics*, 17(2), 171-186,
545 <http://doi.org/10.1029/97TC03411>, 1998.
- Barruol, G. and Kern, H.: Seismic anisotropy and shear-wave splitting in lower-crustal and upper-mantle rocks from the
Ivrea Zone -experimental and calculated data, *Phys. Earth Planet In.*, 95(3-4), 175-194, [https://doi.org/10.1016/0031-9201\(95\)03124-3](https://doi.org/10.1016/0031-9201(95)03124-3), 1996.
- Bastida, F., Aller, J., Pulgar, J. A., Toimil, N. C., Fernández, F. J., Bobillo-Ares, N. C. and Menéndez, C. O.: Folding in
550 orogens: a case study in the northern Iberian Variscan Belt, *Geol. J.*, 45(5-6), 597-622, <https://doi.org/10.1002/gj.1199>, 2010.
- Bastida, F., Martínez-Catalán, J. R. and Pulgar, J. A.: Structural, metamorphic, and magmatic history of the Mondoñedo
nappe (Hercynian belt, NW Spain), *J. Struct. Geol.*, 8(3-4), 415-430, [https://doi:10.1016/0191-8141\(86\)90060-X](https://doi:10.1016/0191-8141(86)90060-X), 1986.
- Bensen, G. D., Ritzwoller, M. H., Barmin, M. P., Levshin, A. L., Lin, F., Moschetti, M. P., Shapiro, N. M. and Yang, Y.:
Processing seismic ambient noise data to obtain reliable broad-band surface wave dispersion measurements, *Geophys. J. Int.*,
555 169(3), 1239-1260, <https://doi.org/10.1111/j.1365-246X.2007.03374.x>, 2007.
- Boillot, G., Dupeuble, P. A. and Malod, J.: Subduction and tectonics on the continental margin off northern Spain, *Mar.
Geol.*, 32(1-2), 53-70, [https://doi.org/10.1016/0025-3227\(79\)90146-4](https://doi.org/10.1016/0025-3227(79)90146-4), 1979.
- Boness, N. L. and Zoback, M. D.: Mapping stress and structurally controlled crustal shear velocity anisotropy in California,
Geology, 34(10), 825-828, <https://doi.org/10.1130/G22309.1>, 2006.
- 560 Brandmayr, E., Kuponiyi, A. P., Arroucau, P. and Vlahovic, G.: Group velocity tomography of the upper crust in the eastern
Tennessee seismic zone from ambient noise data, *Tectonophysics*, 688, 148-156, <https://doi.org/10.1016/j.tecto.2016.09.035>,
2016.
- Cadenas, P. and Fernández-Viejo, G.: The Asturian Basin within the North Iberian margin (Bay of Biscay): seismic
characterisation of its geometry and its Mesozoic and Cenozoic cover, *Basin Res.*, 29(4), 521-541,
565 <https://doi.org/10.1111/bre.12187>, 2017.
- Cadenas, P., Fernández-Viejo, G., Pulgar, J. A., Tugend, J., Manatschal, G. and Minshull, T. A.: Constraints imposed by rift
inheritance on the compressional reactivation of a hyperextended margin: Mapping rift domains in the North Iberian margin
and in the Cantabrian Mountains, *Tectonics*, 37(3), 758-785, <https://doi.org/10.1002/2016TC004454>, 2018.



- 570 Cárdenes, V., Lopez-Sanchez, M. A., Barou, F., Olona, J. and Llana-Fúnez, S.: Crystallographic preferred orientation, seismic velocity and anisotropy in roofing slates, *Tectonophysics*, 808, 228815, <https://doi.org/10.1016/j.tecto.2021.228815>, 2021.
- Chen, Y., Badal, J. and Zhang, Z.: Radial anisotropy in the crust and upper mantle beneath the Qinghai-Tibet Plateau and surrounding regions, *J. Asian Earth Sci.*, 36(4-5), 289-302, <https://doi.org/10.1016/j.jseaes.2009.06.011>, 2009.
- Christensen, N.I.: Measurement of dynamic properties of rock at elevated temperatures and pressures, *American Society of Testing and Materials (ASTM)*. 869, 93-107, <https://doi.org/10.1520/STP32832S>, 1985.
- 575 Crampin, S., Gao, Y. and Bukits, J.: A review of retrospective stress-forecasts of earthquakes and eruptions, *Phys. Earth Planet In.*, 245, 76-87, <http://doi.org/10.1016/j.pepi.2015.05.008>, 2015.
- Crampin, S.: Seismic-wave propagation through a cracked solid: polarization as a possible dilatancy diagnostic, *Geophys. J. Int.*, 53(3), 467-496, <https://doi.org/10.1111/j.1365-246X.1978.tb03754.x>, 1978.
- 580 Crampin, S. and Peacock, S.: A review of shear-wave splitting in the compliant crack-critical anisotropic Earth, *Wave motion*, 41(1), 59-77, <https://doi.org/10.1016/j.wavemoti.2004.05.006v> 2005.
- Díaz, J., Gallart, J., Pedreira, D., Pulgar, J. A., Ruiz, M., López, C. and González-Cortina, J. M.: Teleseismic imaging of alpine crustal underthrusting beneath N Iberia, *Geophys. Res. Lett.*, 30, 1554, <http://doi.org/10.1029/2003GL017073>, 2003.
- Díaz, J., Gallart, J., Ruiz, M., Pulgar, J. A., López-Fernández, C. and González-Cortina, J. M.: Probing seismic anisotropy in 585 North Iberia from shear wave splitting, *Phys. Earth Planet In.*, 158(2-4), 210-225, <https://doi.org/10.1016/j.pepi.2005.12.011>, 2006.
- Díaz, J., Gallart, J., Morais, I., Silveira, G., Pedreira, D., Pulgar, J. A., Días, N. A., Ruiz, M. and González-Cortina, J. M.: From the Bay of Biscay to the High Atlas: Completing the anisotropic characterization of the upper mantle beneath the westernmost Mediterranean region, *Tectonophysics*, 663, 192-202, <http://doi.org/10.1016/j.tecto.2015.03.007>, 2015.
- 590 Díaz, J., Gallart, J., Ruiz, M., Pulgar, J. A. and López-Fernández, C.: Anisotropic features of the Alpine lithosphere in Northern Spain, *Geophys. Res. Lett.*, 29(24), 2225, <http://doi.org/10.1029/2002GL015997>, 2002.
- Díaz, J., Gallart, J., Pulgar, J. A., Ruiz, M. and Pedreira, D.: Crustal structure beneath North-West Iberia imaged using receiver functions, *Tectonophysics*, 478(3-4), 175-183, <http://doi.org/10.1016/j.tecto.2009.08.003>, 2009a.
- Díaz, J., Villaseñor, A., Gallart, J., Morales, J., Pazos, A., Cordoba, D., Pulgar, J. A., Garcia-Lobon, J. L., Harnafi, M. and 595 Topoiberia Seismic Working Group: The IBERARRAY broadband seismic network: A new tool to investigate the deep structure beneath Iberia, *Orfeus Newslett.*, 8(2), 1-6, 2009b.
- Dreiling, J., Tilmann, F., Yuan, X., Giese, J., Rindharisaona, E. J., Rumpker, G. and Wyssession, M. E.: Crustal radial anisotropy and linkage to geodynamic processes: a study based on seismic ambient noise in southern Madagascar, *J. Geophys. Res.-Sol. Ea.*, 123(6), 5130-5146, <https://doi.org/10.1029/2017JB015273>, 2018.
- 600 Dziewonski, A., Bloch, S. and Landisman, M.: A technique for the analysis of transient seismic signals, *B. Seismol. Soc. Am.*, 59(1), 427-444, <https://doi.org/10.1785/BSSA0590010427>, 1969.



- Espina, R.: La estructura y evolución tectonoestratigráfica del borde occidental de la Cuenca Vasco-Cantábrica (Cordillera Cantábrica, NO de España), PhD. Thesis, University of Oviedo, Oviedo, Spain, 1997.
- Fernandez-Viejo, G., Gallart, J., Pulgar, J. A., Gallastegui, J., Dañobeitia, J. J. and Córdoba, D.: Crustal transition between continental and oceanic domains along the North Iberian margin from wide angle seismic and gravity data, *Geophys. Res. Lett.*, 25(23), 4249-4252, <http://doi.org/10.1029/1998GL900149>, 1998.
- Fernández-Viejo, G., Gallart, J., Pulgar, J. A., Córdoba, D. and Dañobeitia, J. J.: Seismic signature of Variscan and Alpine tectonics in NW Iberia: Crustal structure of the Cantabrian Mountains and Duero basin, *J. Geophys. Res.-Sol. Ea.*, 105(B2), 3001-3018, <http://doi.org/10.1029/1999JB900321>, 2000.
- 610 Fernández-Viejo, G. and Gallastegui, J.: The ESCI-N Project after a decade: a synthesis of the results and open questions, *Trabajos Geol.*, (25), 9-27, <https://doi.org/10.17811/TDG.25.2005.9-27>, 2005.
- Fernández-Viejo, G., Gallastegui, J., Pulgar, J. A. and Gallart, J.: The MARCONI project: a seismic view into the eastern part of the Bay of Biscay, *Tectonophysics*, 508, 342-356, <https://doi.org/10.1016/j.tecto.2010.06.020>, 2011.
- Fernández-Viejo, G., Pulgar, J. A., Gallastegui, J. and Quintana, L.: The fossil accretionary wedge of the Bay of Biscay: critical wedge analysis on depth-migrated seismic sections and geodynamical implications, *J. Geol.*, 120(3), 315-331, <http://doi.org/10.1086/664789>, 2012.
- 615 Gallastegui, J.: Estructura cortical de la cordillera y margen continental cantábricos: perfiles ESCI-N, *Trabajos Geol.*, 22, 3-234, <https://doi.org/10.17811/tdg.22.2000.3-234>, 2000.
- Gallastegui, J., Pulgar, J. A. and Alvarez-Marrón, J.: 2-D seismic modeling of the Variscan foreland thrust and fold belt crust in NW Spain from ESCIN-1 deep seismic reflection data, *Tectonophysics*, 269(1-2), 21-32, [https://doi.org/10.1016/S0040-1951\(96\)00166-7](https://doi.org/10.1016/S0040-1951(96)00166-7), 1997.
- 620 Gallastegui, J., Pulgar, J. A. and Gallart, J.: Initiation of an active margin at the North Iberian continent-ocean transition, *Tectonics*, 21(4), 1-15, <https://doi.org/10.1029/2001TC901046>, 2002.
- Godfrey, N. J., Christensen, N. I. and Okaya, D. A.: Anisotropy of schists: Contribution of crustal anisotropy to active source seismic experiments and shear wave splitting observations, *J. Geophys. Res.*, 105(B12), 27991-28007, <https://doi.org/10.1029/2000JB900286>, 2000.
- 625 Guo, Z., Gao, X., Wang, W. and Yao, Z.: Upper-and mid-crustal radial anisotropy beneath the central Himalaya and southern Tibet from seismic ambient noise tomography, *Geophys. J. Int.*, 189(2), 1169-1182, <https://doi.org/10.1111/j.1365-246X.2012.05425.x>, 2012.
- 630 Guo, B.B., Wang, H.C., Zhao, W.H., Ji, S.C., Sun, D.S., Li, A.W. and Long, C.X.: Analysis of Seismic Anisotropy of the Typical Slate from the Gaoligong Mountains, Yunnan Province, China, *Chinese J. G.*, 57(2), 154-165, <https://doi.org/10.1002/cjg2.20093>, 2014.
- Green, R. G., Priestley, K. F. and White, R. S.: 2017 Ambient noise tomography reveals upper crustal structure of Icelandic rifts, *Earth Planet. Sc. Lett.*, 466, 20-31, <https://doi.org/10.1016/j.epsl.2017.02.039>, 2017.



- 635 Gu, N., Wang, K., Gao, J., Ding, N., Yao, H. and Zhang, H.: Shallow crustal structure of the Tanlu Fault Zone near Chao Lake in eastern China by direct surface wave tomography from local dense array ambient noise analysis, *Pure Appl. Geophys.*, 176(3), 1193-1206, <https://doi.org/10.1007/s00024-018-2041-4>, 2019.
- Gutiérrez-Alonso, G.: El Antiforme del Narcea y su relación con los mantos occidentales de la Zona Cantábrica. PhD thesis, University of Oviedo, Oviedo, Spain, 1992.
- 640 Herrmann, R. B.: Computer programs in seismology: An evolving tool for instruction and research, *Seismol. Res. Lett.*, 84(6), 1081-1088, <https://doi.org/10.1785/0220110096>, 2013.
- Ji, S., Shao, T., Michibayashi, K., Oya, S., Satsukawa, T., Wang, Q., Zhao, W. and Salisbury, M. H.: Magnitude and symmetry of seismic anisotropy in mica-and amphibole-bearing metamorphic rocks and implications for tectonic interpretation of seismic data from the southeast Tibetan Plateau, *J. Geophys. Res.*, 120(9), 6404-6430, <https://doi.org/10.1002/2015JB012209>, 2015
- Julivert, M.: Décollement tectonics in the Hercynian Cordillera of northwest Spain, *Am. J. Sci.*, 270(1), 1-29, <https://doi.org/10.2475/ajs.270.1.1>, 1971.
- Kennett, B. L. N., Sambridge, M. S. and Williamson, P. R.: Subspace methods for large inverse problems with multiple parameter classes, *Geophys. J. Int.*, 94(2), 237-247, <https://doi.org/10.1111/j.1365-246X.1988.tb05898.x>, 1988.
- 650 Kern, H.: Laboratory seismic measurements: an aid in the interpretation of seismic field data, *Terra Nova*, 2(6), 617-628, <https://doi.org/10.1111/j.1365-3121.1990.tb00127.x>, 1990.
- Lepvrier, C. and Martínez-García, E.: Fault development and stress evolution of the post-Hercynian Asturian Basin (Asturias and Cantabria, northwestern Spain), *Tectonophysics*, 184(3-4), 345-356, [https://doi.org/10.1016/0040-1951\(90\)90447-G](https://doi.org/10.1016/0040-1951(90)90447-G), 1990.
- 655 Llana-Fúnez, S. and López-Fernández, C.: The seismogenic zone of the continental crust in Northwest Iberia and its relation to crustal structure, *Tectonics*, 34, 1751– 1767, <http://doi.org/10.1002/2015TC003877>, 2015.
- Llana-Fúnez, S. and Marcos, A.: The Malpica–Lamego Line: a major crustal-scale shear zone in the Variscan belt of Iberia, *J. Struct. Geol.*, 23(6-7), 1015-1030, [https://doi.org/10.1016/S0191-8141\(00\)00173-5](https://doi.org/10.1016/S0191-8141(00)00173-5), 2001.
- Llana-Fúnez, S. and Marcos, A.: Convergence in a thermally softened thick crust: Variscan intracontinental tectonics in Iberian plate rocks, *Terra Nova*, 19, 393-400, <https://doi.org/10.1111/j.1365-3121.2007.00763.x>, 2007.
- 660 López-Fernández, C., Fernández-Viejo, G., Olona, J. and Llana-Fúnez, S.: Intraplate Seismicity in Northwest Iberia along the Trace of the Ventaniella Fault: A Case for Fault Intersection at Depth, *B. Seismol. Soc. Am.*; 108 (2), 604–618, <https://doi.org/10.1785/0120170215>, 2018.
- López-Fernández, C., Pulgar, J. A., Díaz, J., Gallart, J., González-Cortina J. M. and Ruiz, M.: Seismotectonic characterization of the Becerreá area (NW Spain), *Geol. Acta*, 10, 71– 80, <http://doi.org/10.1344/105.000001750>, 2012.
- López-Sánchez, M. A., Marcos, A., Martínez, F. J., Iriando, A. and Llana-Fúnez, S.: Setting new constrains on the age of crustal-scale extensional shear zone (Vivero fault): implications for the evolution of Variscan orogeny in the Iberian massif, *Int. J. Earth Sci.*, 104(4), 927-962, <http://doi.org/10.1007/s00531-014-1119-1>, 2015.



- Luo, Y., Xu, Y. and Yang, Y.: Crustal radial anisotropy beneath the Dabie orogenic belt from ambient noise tomography, *Geophys. J. Int.*, 195(2), 1149-1164, <https://doi.org/10.1093/gji/ggt281>, 2013.
- Luo, Y., Yang, Y., Xu, Y., Xu, H., Zhao, K. and Wang, K.: On the limitations of interstation distances in ambient noise tomography, *Geophys. J. Int.*, 201(2), 652-661, <https://doi.org/10.1093/gji/ggv043>, 2015.
- Lynner, C., Beck, S. L., Zandt, G., Porritt, R. W., Lin, F. C. and Eilon, Z. C.: Midcrustal deformation in the Central Andes constrained by radial anisotropy, *J. Geophys. Res.-Sol. Ea.*, 123(6), 4798-4813, <https://doi.org/10.1029/2017JB014936>, 2018.
- Macquet, M., Paul, A., Pedersen, H. A., Villaseñor, A., Chevrot, S., Sylvander, M., Wolyniec, D. and PYROPE Working Group.: Ambient noise tomography of the Pyrenees and the surrounding regions: inversion for a 3-D Vs model in the presence of a very heterogeneous crust, *Geophys. J. Int.*, 199(1), 402-415, <https://doi.org/10.1093/gji/ggu270>, 2014.
- Mancilla, F. and Diaz, J.: High resolution Moho topography map beneath Iberia and Northern Morocco from receiver function analysis, *Tectonophysics*, 663, 203-211, <https://doi.org/10.1016/j.tecto.2015.06.017>, 2015.
- Marcos, A.: Las series del Paleozoico Inferior y la estructura herciniana del Occidente de Asturias (NW. de España), *Trabajos Geol.*, 6(6), 3-113, <https://doi.org/10.17811/tdg.6.1973.3-113>, 1973.
- Marcos, A.: Un nuevo mapa geológico de la parte septentrional del Domo de Lugo (Galicia oriental, NO de España): Implicaciones sobre la estratigrafía, estructura y evolución tectónica del Manto de Mondoñedo, *Trabajos Geol.*, 33, 171-200, 2013.
- Marcos, A., Fariás, P., Galán, G., Fernández, F. J. and Llana-Fúnez, S.: Tectonic framework of the Cabo Ortegal Complex: A slab of lower crust exhumed in the Variscan orogen (northwestern Iberian Peninsula), *Geological Society of America Special Papers*, 364, 143-162, <https://doi.org/10.1130/0-8137-2364-7.143>, 2002.
- Marcos, A., and Pulgar, J. A.: An approach to the tectonostratigraphic evolution of the Cantabrian foreland thrust and fold belt, Hercynian Cordillera of NW Spain, *Neues Jahrbuch für Geologie und Paläontologie. Abhandlungen*, 163(2), 256-260, 1982.
- Martínez-Catalán, J.R., Arenas, R., Abati, J., Sánchez Martínez, S., Díaz-García, F., Fernández-Suárez, J., González-Cuadra, P., Castiñeiras, P., Gómez-Barreiro, J., Díez-Montes, A., González-Clavijo, E., Rubio-Pascual, F. J., Andonaegui P., Jeffries, T. E., Alcock, J. E., Díez-Fernández, R. and López-Carmona, A.: A rootless suture and the loss of the roots of a mountain chain: the Variscan belt of NW Iberia, *Comptes Rendus Geosci.*, 341, 114–126, <http://doi.org/10.1016/j.crte.2008.11.004>, 2009.
- Martínez-Catalán, J. R., Arenas, R., Díaz García, F. and Abati, J.: Variscan accretionary complex of northwest Iberia: Terrane correlation and succession of tectonothermal events, *Geology*, 25(12), 1103-1106, [https://doi.org/10.1130/0091-7613\(1997\)025%3C1103:VACONI%3E2.3.CO;2](https://doi.org/10.1130/0091-7613(1997)025%3C1103:VACONI%3E2.3.CO;2), 1997.
- Martínez-Catalán, J. R., Álvarez-Lobato, F., Pinto, V., Gómez-Barreiro, J., Ayarza, P., Villalán, J. J. and Casas, A.: Gravity and magnetic anomalies in the allochthonous Órdenes Complex (Variscan belt, northwest Spain): Assessing its internal structure and thickness, *Tectonics*, 31, TC5007, <https://doi.org/10.1029/2011TC003093>, 2012.



- Martín-González, F., Barbero, L., Capote, R., Heredia, N. and Gallastegui, G.: Interaction of two successive Alpine deformation fronts: constraints from low temperature thermochronology and structural mapping (NW Iberian Peninsula), *Int. J. Earth Sci.*, 101(5), 1331-1342, <http://doi.org/10.1007/s00531-011-0712-9>, 2012.
- Matte, P.: La structure de la virgation hercynienne de Galice (Espagne), Allier, Grenoble, France, 1968.
- Matte, P.: Tectonics and plate tectonics model for the Variscan belt of Europe, *Tectonophysics*, 126(2-4), 329-374, [https://doi.org/10.1016/0040-1951\(86\)90237-4](https://doi.org/10.1016/0040-1951(86)90237-4), 1986.
- Merino-Tomé, O. A., Bahamonde, J. R., Colmenero, J. R., Heredia, N., Villa, E. and Farias, P.: Emplacement of the Cuera and Picos de Europa imbricate system at the core of the Iberian-Armorican arc (Cantabrian zone, north Spain): New precisions concerning the timing of arc closure, Emplacement of the Cuera Unit and the Picos de Europa, *GSA Bull.*, 121(5-6), 729-751, <https://doi.org/10.1130/B26366.1>, 2009.
- Moschetti, M. P., Ritzwoller, M. H., Lin, F. and Yang, Y.: Seismic evidence for widespread western-US deep-crustal deformation caused by extension, *Nature*, 464(7290), 885-889, <https://doi.org/10.1038/nature08951>, 2010.
- Naghavi, M., Hatami, M., Shirzad, T. and Rahimi, H.: Radial anisotropy in the Upper Crust beneath the Tehran Basin and surrounding regions, *Pure Appl. Geophys.*, 176(2), 787-800, <https://link.springer.com/article/10.1007/s00024-018-1986-7>, 2019.
- Nicolson, H., Curtis, A. and Baptie, B.: Rayleigh wave tomography of the British Isles from ambient seismic noise, *Geophys. J. Int.*, 198(2), 637-655, <https://doi.org/10.1093/gji/ggu071>, 2014.
- Nicolson, H., Curtis, A., Baptie, B. and Galetti, E.: Seismic interferometry and ambient noise tomography in the British Isles, *P. Geologist. Assoc.*, 123(1), 74-86, <https://doi.org/10.1016/j.pgeola.2011.04.002>, 2012.
- Ojo, A. O., Ni, S. and Li, Z.: Crustal radial anisotropy beneath Cameroon from ambient noise tomography, *Tectonophysics*, 696, 37-51, <http://doi.org/10.1016/j.tecto.2016.12.018>, 2017.
- Olivar-Castaño, A., Pilz, M., Pedreira, D., Pulgar, J. A., Díaz-González, A. and González-Cortina, J. M.: Regional Crustal Imaging by Inversion of Multimode Rayleigh Wave Dispersion Curves Measured from Seismic Noise: Application to the Basque-Cantabrian Zone (N Spain), *J. Geophys. Res.-Sol. Ea.*, 125(12), e2020JB019559, <https://doi.org/10.1029/2020JB019559>, 2020.
- Palomeras, I., Villaseñor, A., Thurner, S., Levander, A., Gallart, J. and Harnafi, M.: Lithospheric structure of Iberia and Morocco using finite-frequency Rayleigh wave tomography from earthquakes and seismic ambient noise, *Geochem. Geophys. Geosy.*, 18(5), 1824-1840, <http://doi.org/10.1002/2016GC006657>, 2017.
- Pastor-Galán, D., Gutiérrez-Alonso, G., Murphy, J. B., Fernández-Suárez, J., Hofmann, M. and Linnemann, U.: Provenance analysis of the Paleozoic sequences of the northern Gondwana margin in NW Iberia: Passive margin to Variscan collision and orocline development, *Gondwana Res.*, 23(3), 1089-1103, <https://doi.org/10.1016/j.gr.2012.06.015>, 2013.
- Pastor-Galán, D., Gutiérrez-Alonso, G. and Weil, A. B.: Orocline timing through joint analysis: Insights from the Ibero-Armorican Arc, *Tectonophysics*, 507(1-4), 31-46, <https://doi.org/10.1016/j.tecto.2011.05.005>, 2011.



- Pedreira, D., Afonso, J. C., Pulgar, J. A., Gallastegui, J., Carballo, A., Fernandez, M., García-Castellanos, D., Jiménez-Munt, I., Semprich, J. and Garcia-Moreno, O.: Geophysical-petrological modelling of the lithosphere beneath the Cantabrian Mountains and the North-Iberian margin: Geodynamic implications, *Lithos*, 230, 46-68, <http://doi.org/10.1016/j.lithos.2015.04.018>, 2015.
- 740 Pérez-Estaún, A., Bastida, F., Alonso, J. L., Marquínez, J., Aller, J., Alvarez-Marrón, J., Marcos, A. and Pulgar, J. A.: A thin-skinned tectonics model for an arcuate fold and thrust belt: the Cantabrian Zone (Variscan Ibero-Armorican Arc), *Tectonics*, 7(3), 517-537, <http://doi.org/10.1029/TC007i003p00517>, 1988.
- Pérez-Estaún, A., Martínez Catalán, J.R. and Bastida, F.: Crustal thickening and deformation sequence in the footwall to the suture of the Variscan belt of northwest Spain, *Tectonophysics*, 191: 243-253, [https://doi.org/10.1016/0040-1951\(91\)90060-](https://doi.org/10.1016/0040-1951(91)90060-6)
745 6, 1991.
- Pérez-Estaún, A., Pulgar, J. A., Banda, E., Álvarez-Marrón, J., and Esci-N Research Group.: Crustal structure of the external variscides in northwest Spain from deep seismic reflection profiling, *Tectonophysics*, 232(1-4), 91-118, [https://doi.org/10.1016/0040-1951\(94\)90078-7](https://doi.org/10.1016/0040-1951(94)90078-7), 1994.
- Pulgar, J. A., Alonso, J. L., Espina, R. G. and Marín, J. A.: La deformación alpina en el basamento varisco de la Zona
750 Cantábrica, *Trabajos Geol.*, 21, 283-294, 1999.
- Pulgar, J. A., Gallart, J., Fernández-Viejo, G., Pérez-Estaún, A., Álvarez-Marrón, J. and Escin Group.: Seismic image of the Cantabrian Mountains in the western extension of the Pyrenees from integrated ESCIN reflection and refraction data, *Tectonophysics*, 264(1-4), 1-19, [https://doi.org/10.1016/S0040-1951\(96\)00114-X](https://doi.org/10.1016/S0040-1951(96)00114-X), 1996.
- Pulgar, J. A., Pérez-Estaún, A., Gallart, J., Álvarez-Marrón, J. and Gallastegui, J.: The ESCI-N2 deep seismic reflection
755 profile: a traverse across the Cantabrian Mountains and adjacent Duero basin, *Rev. Soc. Geol. España*, 8, 4, 1995.
- Rawlinson, N.: FMST: fast marching surface tomography package—Instructions. Research School of Earth Sciences, Australian National University, Canberra, Australia, 2005.
- Rawlinson, N. and Sambridge, M.: Wave front evolution in strongly heterogeneous layered media using the fast-marching method, *Geophys. J. Int.*, 156(3), 631-647, <https://doi.org/10.1111/j.1365-246X.2004.02153.x>, 2004a.
- 760 Rawlinson, N. and Sambridge, M.: Multiple reflection and transmission phases in complex layered media using a multistage fast marching method, *Geophysics*, 69(5), 1338-1350, <https://doi.org/10.1190/1.1801950>, 2004b.
- Ribeiro, A., Munhá, J., Dias, R., Mateus, A., Pereire, E., Ribeiro, L., Fonseca, P., Araújo, A., Oliveira, T., Romão, J., Chaminé, H., Coke, C. and Pedro, J.: Geodynamic evolution of the SW Europe Variscides, *Tectonics*, 26, TC6009, <https://doi.org/10.1029/2006TC002058>, 2007.
- 765 Rubio-Ordóñez, A., Gutiérrez-Alonso, G., Valverde-Vaquero, P., Cuesta, A., Gallastegui, G., Gerdes, A. and Cárdenes, V.: Arc-related Ediacaran magmatism along the northern margin of Gondwana: Geochronology and isotopic geochemistry from northern Iberia, *Gondwana Res.*, 27(1), 216-227, <https://doi.org/10.1016/j.gr.2013.09.016>, 2015.
- Sammarco, C., Cornwell, D. G. and Rawlinson, N.: Ambient noise tomography reveals basalt and sub-basalt velocity structure beneath the Faroe Islands, North Atlantic, *Tectonophysics*, 721, 1-11, <http://doi.org/10.17863/CAM.20927>, 2017.



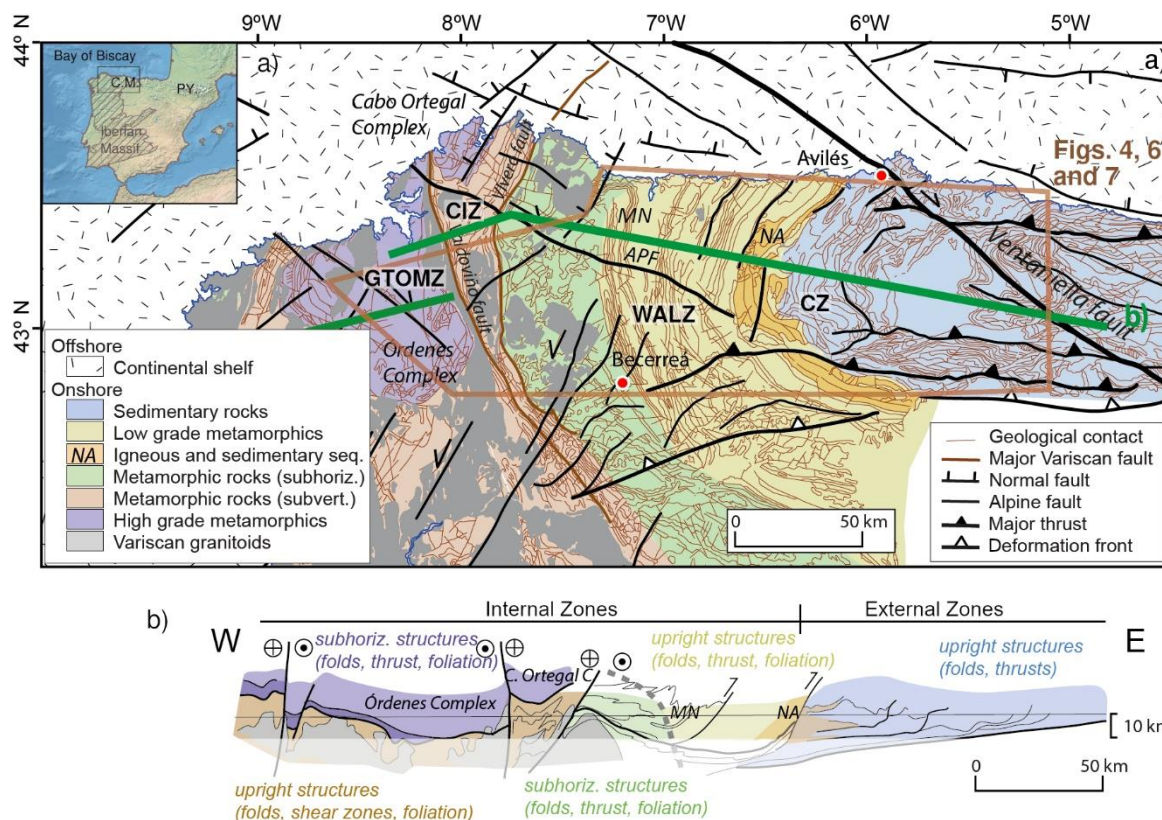
- 770 Savage, M. K.: Lower crustal anisotropy or dipping boundaries? Effects on receiver functions and a case study in New Zealand, *J. Geophys. Res.-Sol. Ea.*, 103(B7), 15069-15087, <https://doi.org/10.1029/98JB00795>, 1998.
- Schimmel, M.: Phase cross-correlations: Design, comparisons, and applications, *B. Seismol. Soc. Am.*, 89(5), 1366-1378, <https://doi.org/10.1785/BSSA0890051366>, 1999.
- Schimmel, M. and Gallart, J.: Frequency-dependent phase coherence for noise suppression in seismic array data, *J. Geophys. Res.-Sol. Ea.*, 112(B4), <https://doi.org/10.1029/2006JB004680>, 2007.
- 775 Schimmel, M., Stutzmann, E. and Gallart, J.: Using instantaneous phase coherence for signal extraction from ambient noise data at a local to a global scale, *Geophys. J. Int.*, 184(1), 494-506, <https://doi.org/10.1111/j.1365-246X.2010.04861.x>, 2011.
- Sethian, J. A.: A fast-marching level set method for monotonically advancing fronts, *P. Nat. A. Sci. USA*, 93(4), 1591-1595, <https://doi.org/10.1073/pnas.93.4.1591>, 1996.
- 780 Shapiro, N. M. and Campillo, M.: Emergence of broadband Rayleigh waves from correlations of the ambient seismic noise, *Geophys. Res. Lett.*, 31(7), L07614, <https://doi.org/10.1029/2004GL019491>, 2004.
- Shapiro, N. M., Campillo, M., Stehly, L. and Ritzwoller, M. H.: High-resolution surface-wave tomography from ambient seismic noise, *Science*, 307(5715), 1615-1618, <http://doi.org/10.1126/science.1108339>, 2005.
- Shirzad, T. and Shomali, Z. H.: Shallow crustal radial anisotropy beneath the Tehran basin of Iran from seismic ambient noise tomography, *Phys. Earth Planet In.*, 231, 16-29, <https://doi.org/10.1016/j.pepi.2014.04.001>, 2014.
- 785 Shirzad, T., Shomali, Z. H., Riahi, M. A. and Jarrahi, M.: Near surface radial anisotropy in the Rigan area/SE Iran, *Tectonophysics*, 694, 23-34, <http://doi.org/10.1016/j.tecto.2016.11.036>, 2017.
- Silveira, G., Dias, N. A. and Villaseñor, A.: Seismic imaging of the western Iberian crust using ambient noise: Boundaries and internal structure of the Iberian Massif, *Tectonophysics*, 589, 186-194, <http://doi.org/10.1016/j.tecto.2012.12.025>, 2013.
- 790 Snieder, R.: Extracting the Green's function from the correlation of coda waves: A derivation based on stationary phase, *Phys. Rev. E*, 69(4), 046610, <https://doi.org/10.1103/PhysRevE.69.046610>, 2004.
- Tavani, S., Quintà, A. and Granado, P.: Cenozoic right-lateral wrench tectonics in the Western Pyrenees (Spain): the Ubierna Fault System, *Tectonophysics*, 509(3-4), 238-253, <https://doi.org/10.1016/j.tecto.2011.06.013>, 2011.
- 795 Teixell, A., Labaume, P., Ayarza, P., Espurt, N., de Saint Blanquat, M. and Lagabriele, Y.: Crustal structure and evolution of the Pyrenean-Cantabrian belt: A review and new interpretations from recent concepts and data, *Tectonophysics*, 724, 146-170, <https://doi.org/10.1016/j.tecto.2018.01.009>, 2018.
- Tugend, J., Manatschal, G. and Kuszniir, N. J.: Spatial and temporal evolution of hyperextended rift systems: Implication for the nature, kinematics, and timing of the Iberian-European plate boundary, *Geology*, 43(1), 15-18, <https://doi.org/10.1130/G36072.1>, 2015.
- 800 Uzkeda, H., Bulnes, M., Poblet, J., García-Ramos, J. C. and Piñuela, L.: Buttressing and reverse reactivation of a normal fault in the Jurassic rocks of the Asturian Basin, NW Iberian Peninsula, *Tectonophysics*, 599, 117-134, <http://doi.org/10.1016/j.tecto.2013.04.012>, 2013.



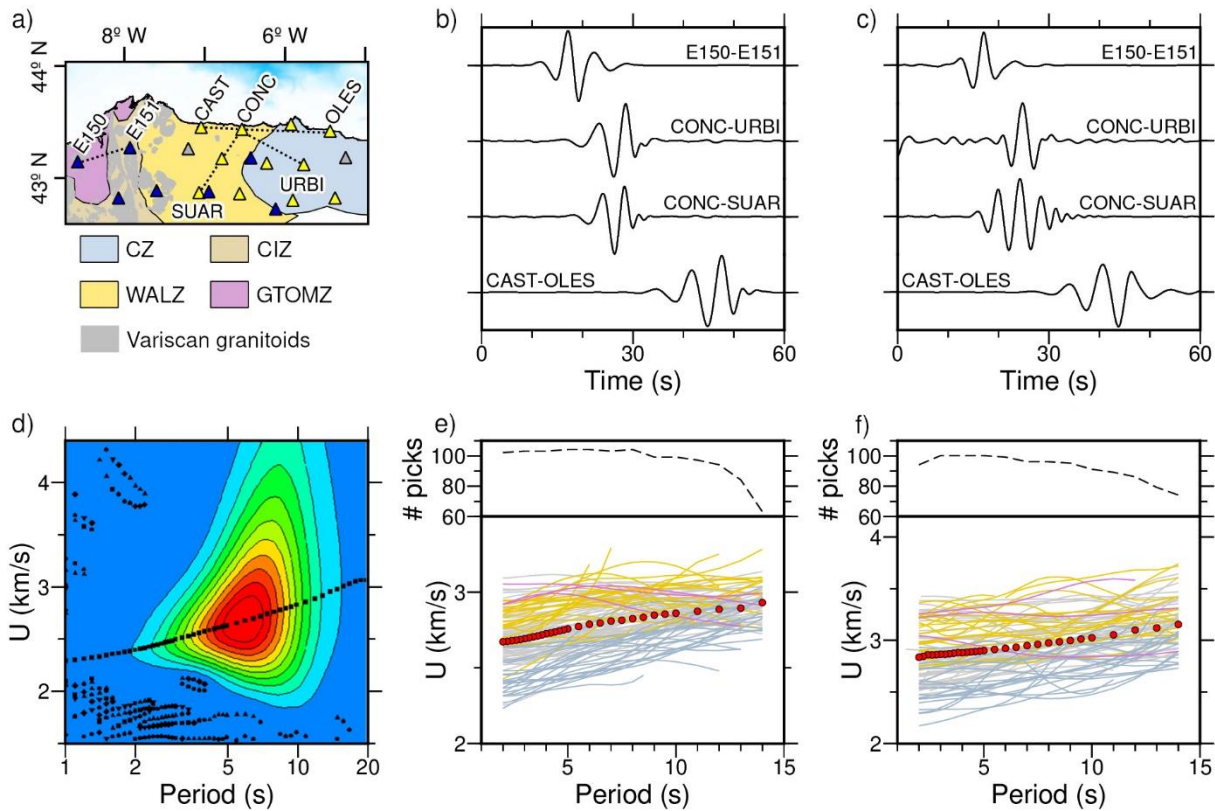
- Wang, J., Gu, Y. J. and Chen, Y.: Shear velocity and radial anisotropy beneath southwestern Canada: Evidence for crustal extension and thick-skinned tectonics, *J. Geophys. Res. - Sol. Ea.*, 125(2), e2019JB018310, 805 <https://doi.org/10.1029/2019JB018310>, 2020.
- Wapenaar, K.: Synthesis of an inhomogeneous medium from its acoustic transmission response, *Geophysics*, 68(5), 1756-1759, <https://doi.org/10.1190/1.1620649>, 2003.
- Wapenaar, K.: Retrieving the elastodynamic Green's function of an arbitrary inhomogeneous medium by cross correlation, *Phys. Rev. Lett.*, 93(25), 254301, <https://doi.org/10.1103/PhysRevLett.93.254301>, 2004.
- 810 Wenk, H. R., Yu, R., Cárdenes, V., Lopez-Sanchez, M. A. and Sintubin, M.: Fabric and anisotropy of slates: From classical studies to new results, *J. Struct. Geol.*, 104066, <https://doi.org/10.1016/j.jsg.2020.104066>, 2020.
- Wessel, P. and Smith, W. H.: New, improved version of Generic Mapping Tools released, *Eos. T. Am. Geophys. Un.*, 79(47), 579-579, <https://doi.org/10.1029/98EO00426>, 1998.
- 815 Xie, J., Ritzwoller, M. H., Shen, W., Yang, Y., Zheng, Y. and Zhou, L.: Crustal radial anisotropy across eastern Tibet and the western Yangtze craton, *J. Geophys. Res.-Sol. Ea.*, 118(8), 4226-4252, <https://doi.org/10.1002/jgrb.50296>, 2013.
- Yanovskaya, T. B., Kizima, E. S. and Antonova, L. M.: Structure of the crust in the Black Sea and adjoining regions from surface wave data, *J. Seismol.*, 2(4), 303-316, <https://doi:10.1023/A:1009716017960>, 1998.
- Zinke, J. C. and Zoback, M. D.: Structure-related and stress-induced shear-wave velocity anisotropy: observations from microearthquakes near the Calaveras Fault in Central California, *B. Seismol. Soc. Am.*, 90(5), 1305-1312, 820 <https://doi:10.1785/0119990099>, 2000.



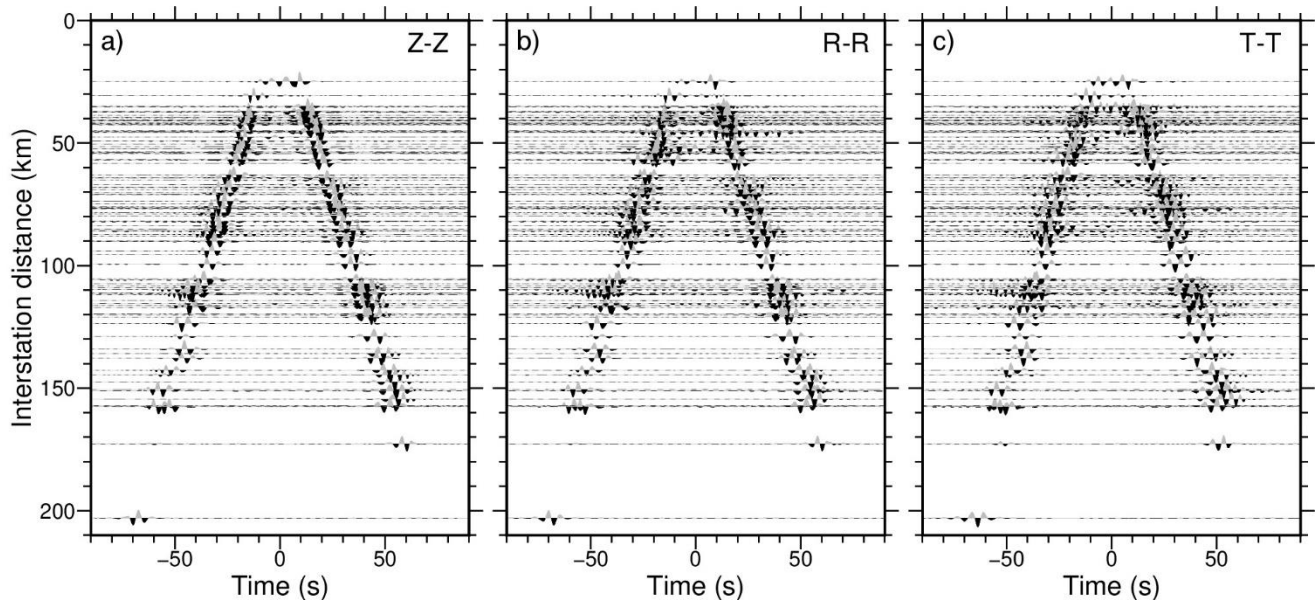
Figures



825 **Figure 1:** (a) Simplified geological map of the study area showing a lithological zonation of the Iberian Variscan orogen in NW
 830 Spain. The green line marks the position of the cross-sections in Figs. 1b, 8 and 9. (Inset) Location of the investigated area within
 the Iberian Peninsula and the Variscan Iberian Massif. CZ: Cantabrian Zone, WALZ: West-Asturian Leonese Zone, CIZ:
 Central-Iberian Zone, GTOMZ: Galicia-Trás-os-Montes Zone. APF: As Pontes fault, MN: Mondoñedo nappe, NA: Narcea
 antiform, PY: Pyrenees, CM: Cantabrian Mountains. Background geology onshore is taken from the continuous geological map of
 Spain at 1:1000000 (IGME). (b) General cross-section across the northwestern Iberian Variscan belt (based on Pérez-Estaún *et al.*,
 1991). The opaque part of the profile highlights the sampled depth in this study.

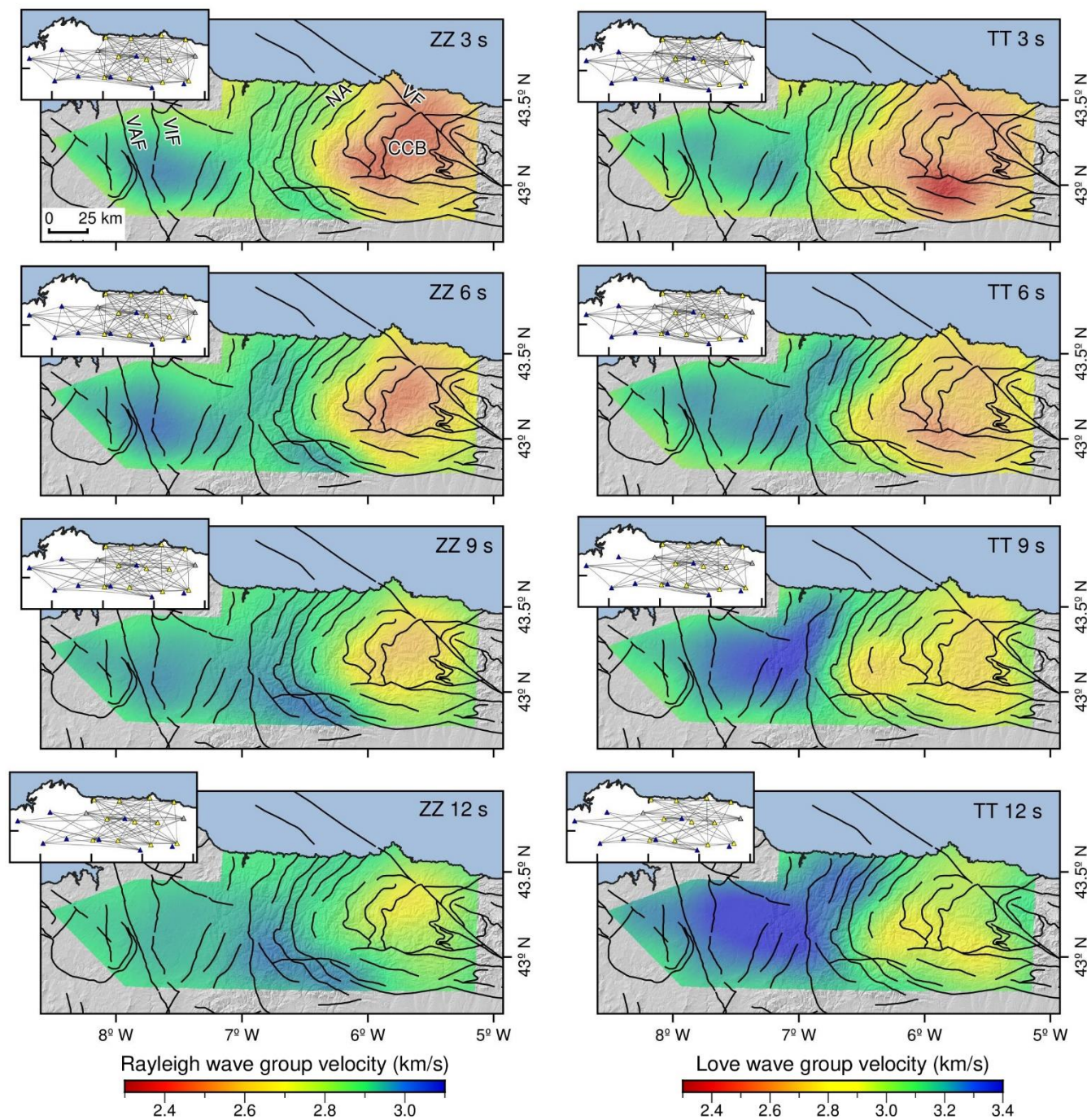


835 **Figure 2:** (a) Location of the displayed interstation paths. Triangles represent the position of the seismic stations that were used in
 this study, belonging to the GEOCSN (yellow triangles), SSN (grey triangles) and IberArray (blue triangles) networks. (b)
 Examples of stacked vertical and (c) transverse component symmetric EGFs. Rayleigh and Love waves are the dominant phases,
 respectively. (d) Example of MFA surface for the CONC-URBI (vertical component) station pair, showing the fundamental mode
 Rayleigh-wave group velocity dispersion curve. (e) Rayleigh- and (f) Love-wave group velocity dispersion curves showing the
 840 number of velocity estimations used in the inversion as a function of the period. Dispersion curves obtained for paths fully
 contained within the main geological domains are highlighted using the colours in Fig. 2a, except for paths crossing the CIZ,
 GTOMZ or both, which are indistinctly marked in pink. Grey dispersion curves represent mixed paths that span through more
 than one region. Red circles illustrate the average dispersion values used in the computation of the initial regional S-wave velocity
 models. U: group velocity.

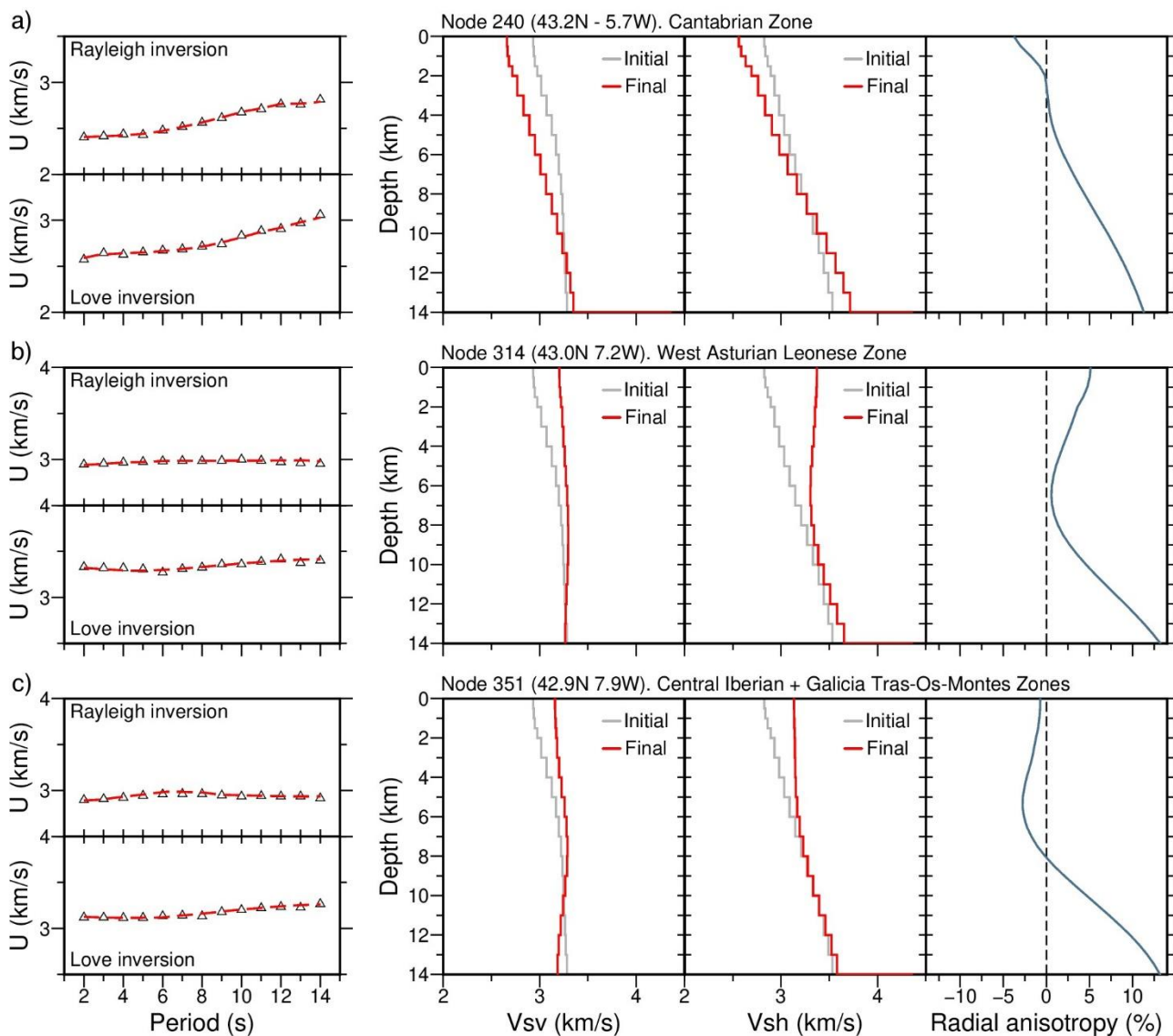


845

Figure 3: Record sections showing the EGFs of all the available station pairs obtained from the cross-correlation of the a) vertical (Z-Z), b) radial (R-R) and c) transverse (T-T) components.



850 **Figure 4: Rayleigh (left panels) and Love (right panels) group velocity tomographic maps for 3, 6, 9 and 12 s periods. Black lines represent the main Alpine and Variscan faults. Insets depict the interstation paths used in each inversion. CCB: Central Coal basin, NA: Narcea antiform, VF: Ventaniella fault, VIF: Vivero fault, VAF: Valdoviño fault.**



855 **Figure 5: Depth inversion results in three nodes of the grid located in different geological domains of the Iberian Variscan orogen.** Left panels display the observed group velocity data (triangles) and the inverted model fit to the dispersion (dashed red line). Central panels show the initial and final S-wave velocity models from Rayleigh (left) and Love (right) waves, respectively. Panels to the right depict the radial anisotropy magnitude calculated with Equation 1. (a) Example of inversion result in the Cantabrian Zone. (b) Example of inversion result in the West Asturian Leonese Zone. (c) Example of inversion result in the Central Iberian / Galicia Tras-Ós-Montes Zones. U: group velocity.

860

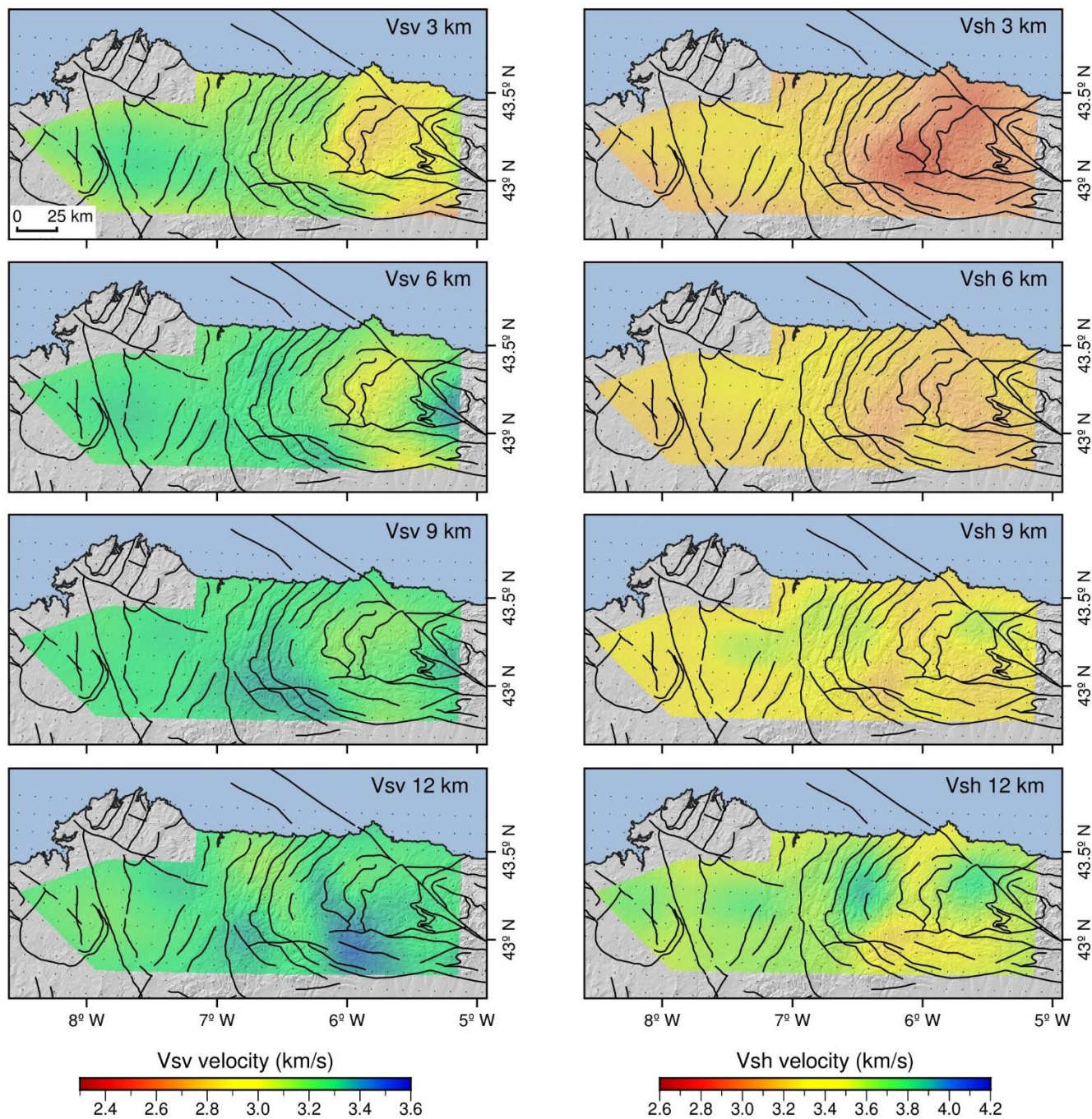
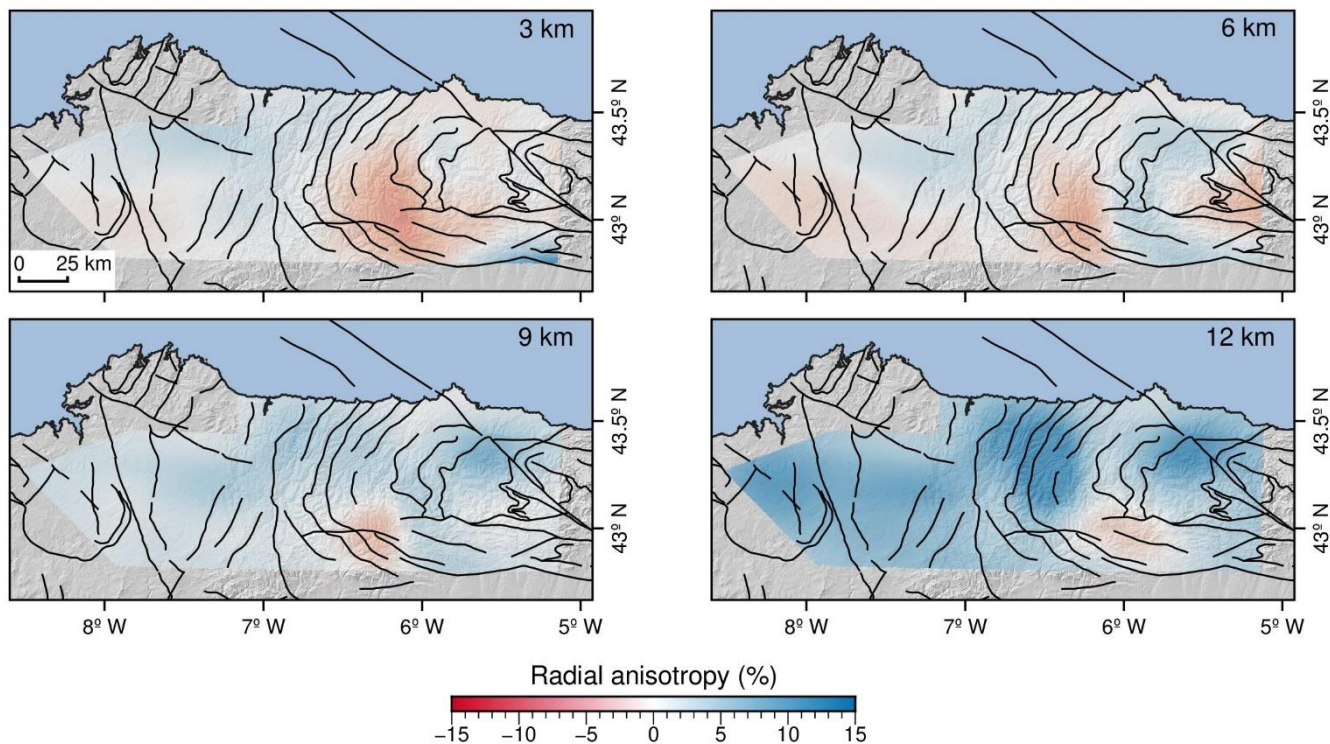
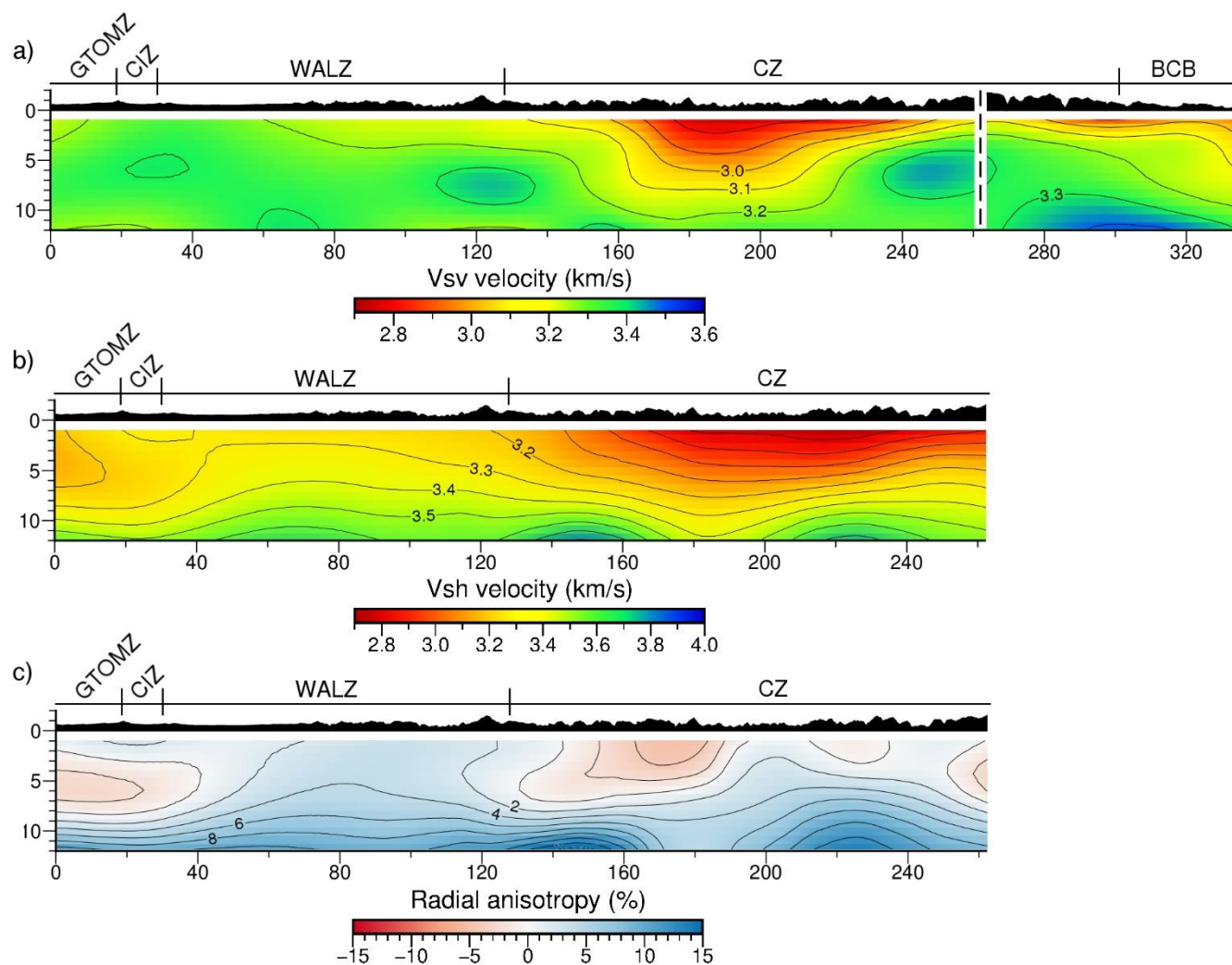


Figure 6: Inverted V_{sv} (left panels) and V_{sh} (right panels) velocity tomographic maps for depths of 3, 6, 9 and 12 km. Black lines represent the main Alpine and Variscan faults. The point grid marks the position of each inverted V_s depth model.

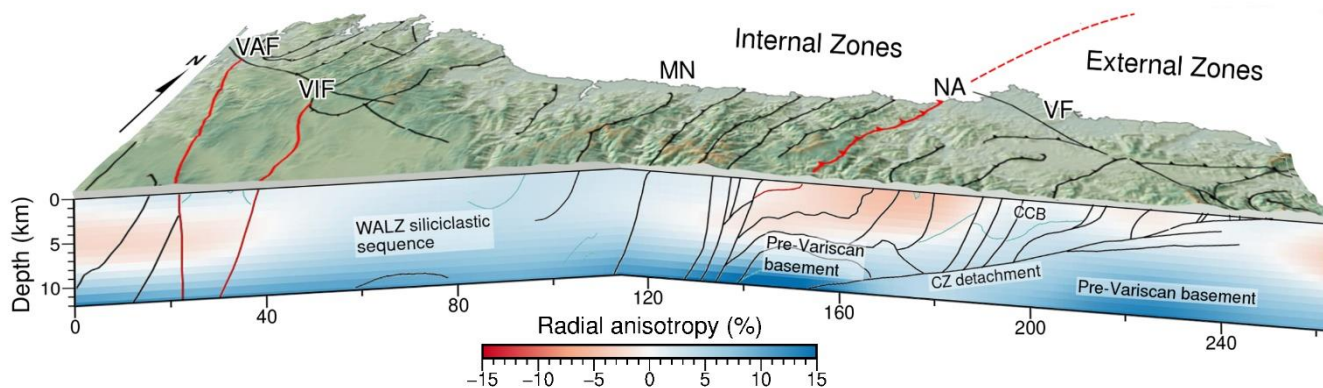


865

Figure 7: Radial anisotropy maps for depths of 3, 6, 9 and 12 km. Black lines represent the main Alpine and Variscan faults.



870 **Figure 8: Cross-section through the (a) V_{sv} , (b) V_{sh} and (c) radial anisotropy models (location in Fig. 1), showing the topographic relief and the limits of the main geological domains. The V_{sv} cross-section has been extended to the East using the model in Acevedo et al. (2019).**



875 **Figure 9:** Schematic 3D block showing the upper-crustal radial anisotropy variation across an E-W transect of the upper crust in NW Iberia. The main structural features are superimposed, based on Pérez-Estaún et al. (1991). Red lines indicate the structures that bound the main Variscan domains displayed in Fig. 1. The location of the cross-section is highlighted in Fig. 1a. CCB: Central Coal basin, VF: Ventaniella fault, MN: Mondoñedo nappe, VIF: Vivero fault, VAF: Valdoviño fault.